Mechanical Systems and Signal Processing 106 (2018) 334–354

Contents lists available at ScienceDirect

Mechanical Systems and Signal Processing

journal homepage: www.elsevier.com/locate/ymssp

Vibration control of multiferroic fibrous composite plates using active constrained layer damping

S.C. Kattimani *, M.C. Ray

Department of Mechanical Engineering, National Institute of Technology Karnataka, Surathkal 575025, India
Department of Mechanical Engineering, Indian Institute of Technology, Kharagpur 721302, India

ARTICLE INFO

Article history:
Received 9 September 2017
Received in revised form 17 November 2017
Accepted 22 December 2017

Keywords:
Magneto-electro-elastic
FRMEE composite
Multiferroic composite
Active constrained layer damping (ACLD)
Geometrically nonlinear vibrations (GNV)

ABSTRACT

Geometrically nonlinear vibration control of fiber reinforced magneto-electro-elastic or multiferroic fibrous composite plates using active constrained layer damping treatment has been investigated. The piezoelectric ($BaTiO_3$) fibers are embedded in the magnetostrictive ($CoFe_2O_4$) matrix forming magneto-electro-elastic or multiferroic smart composite. A three-dimensional finite element model of such fiber reinforced magneto-electro-elastic plates integrated with the active constrained layer damping patches is developed. Influence of electro-elastic, magneto-elastic and electromagnetic coupled fields on the vibration has been studied. The Golla–Hughes–McTavish method in time domain is employed for modeling a constrained viscoelastic layer of the active constrained layer damping treatment. The von Kármán type nonlinear strain-displacement relations are incorporated for developing a three-dimensional finite element model. Effect of fiber volume fraction, fiber orientation and boundary conditions on the control of geometrically nonlinear vibration of the fiber reinforced magneto-electro-elastic plates is investigated. The performance of the active constrained layer damping treatment due to the variation of piezoelectric fiber orientation angle in the 1–3 Piezoelectric constraining layer of the active constrained layer damping treatment has also been emphasized.

1. Introduction

A novel class of multiphase composite made of ferroelectric material $BaTiO_3$ (barium titanate) and ferromagnetic material $CoFe_2O_4$ (cobalt ferrite) is generally called as multiferroic or Magneto-electro-elastic (MEE) composites. Because of the distinct prosperities, multiferroic composites have received significant attention in the field of micro-electro-mechanical systems (MEMS). The ability of MEE composites can be visualized as a process of transfer of energy among the magnetic domain, mechanical domain and the electric domain exhibiting the coupling between electro-mechanical, magneto-mechanical and electromagnetic fields. The superior properties of MEE composites may be utilized for various smart structural applications apart from aeronautical industries. Such as sensors, actuators, transducers, spintronics, micro-electro-mechanical systems, ultrasonic image devices etc. Studies concerned with multiferroic effect and/or MEE structures have been received more attention from the researchers. Pan [1] was the first to study the exact solutions MEE plates while Pan and Heyliger [2] studied the free vibration analysis of MEE plates using modified Stroh formalism and propagator matrix method. Buchanan [3] computed the natural frequencies of vibration for MEE layered infinite plate and compared with

* Corresponding author.
E-mail address: sck@nitk.ac.in (S.C. Kattimani).

https://doi.org/10.1016/j.ymssp.2017.12.039
0888-3270/

multiphase composite plates. Large deflection in thin flexible structures is an important factor which needs an extra care in the design of thin flexible structure used in the aerospace, automotive, medical image devices and precision instruments. Considerable research is being devoted to studying the large deflection of MEE plates recently. Xue et al. [4] proposed the analytical solutions for the large-deflection model of rectangular MEE thin plate under the action of a transverse static mechanical load. They observed that coupling effect on the deflection is negligible for the MEE plate made of different volume fractions of the piezoelectric and piezomagnetic phases. Sladek et al. [5] proposed the meshless local Petrov-Galerkin method to analyze the large deformation of MEE thick plates under the static and time-harmonic mechanical load and stationary electromagnetic load. Alaimo et al. [6] proposed an equivalent single-layer model for the large deflection analysis of multilayered MEE laminates by finite element (FE) method. Milazzo [7,8] analyzed the large deflection of MEE laminated plates using von Kármán stress function approach. Kattimani and Ray [9,10] studied the active control of large amplitude vibrations of MEE plates and doubly curved shells using 1–3 piezoelectric composites. Chen and Yu [11] developed the geometrically nonlinear multiphysics plate model and analyzed the MEE laminated composites by applying the variational asymptotic method. Shooshtari and Razavi [12] studied the nonlinear vibration of a transversely isotropic simply supported MEE thin plate based on the thin plate theory. Zhou and Zhu [13] used the third-order shear deformation theory to analyze the vibration and bending of multiferroic rectangular plates. Geometrically nonlinear vibration analysis of multiferroic composite plates and shells has been studied by Kattimani [14]. Further, effect aspect ratio on the nonlinear amplitude ratio and central deflection has been investigated. The backbone curves depicting the nonlinearity in the multiferroic composite plates and shells for different stacking sequence has been studied.

The magneto-electro-elastic effect in the composite can be obtained by combining the piezoelectric and the piezomagnetic components either in a single layer with functionally graded materials or multilayered with a combination of piezoelectric and piezomagnetic materials. In addition, the MEE effect can also be achieved by the piezoelectric fiber reinforced in the piezomagnetic matrix [15]. Among the few materials which possess the piezoelectric/piezomagnetic properties, the composite made of barium titanate ($BaTiO_3$) and cobalt ferrite ($CoFe_2O_4$) exhibit significantly high electromagnetic coupling effect in comparison to individual constituents [16]. The MEE composite in which the substrate layer is composed of piezoelectric/piezomagnetic fiber reinforced in the piezomagnetic/piezoelectric matrix is commonly referred as fiber-reinforced magneto-electro-elastic (FRMEE) composites. If the fibers are made of a piezoelectric ($BaTiO_3$) material, the matrix is piezomagnetic ($CoFe_2O_4$) and vice versa. The effective material properties of such composites (FRMEE) are expressed by different volume fractions of the piezoelectric constituent ($BaTiO_3$) in FRMEE composites [17]. The micromechanics methods of determining the effective material properties of such composites have gained the remarkable attention of the researchers/scien tist/engineers in recent years [18-22]. In addition, the behavior of the crack in the magneto-electro-elastic medium has been studied by Wang and Mai [23]. Fracture analysis of cracked 2D planar and axiymmetric problems of magneto-electro-elastic material is studied by Li et al. [24] using meshless local Petrov–Galerkin (MLPG) coupled with finite element method (FEM).

A structure can be made to possess a self-sensing and self-controlling capabilities by incorporating a very thin layer of smart materials within the structure or bonded on the surface of the structure. It is due to the fact that the inherent property of piezoelectric/piezomagnetic smart materials which exhibit electro-elastic or magneto-elastic coupling. The structures integrated with such smart materials and showing a self-sensing and self-controlling capabilities are conventionally called as smart structures or intelligent structures. It may be noted that the properties of monolithic piezoelectric materials can be improved significantly by forming composite made with the piezoelectric fibers reinforced in an epoxy matrix. Such composites are generally called as active damping piezoelectric composites. However, in order to enhance the controlling capability further, the active constrained layer damping (ACLD) treatment has been developed [25]. In a typical ACLD treatment, the low stiff constrained viscoelastic layer is sandwiched between the substrate (host structure) and the 1–3 PZC active constraining layer to produce high shear deformation, resulting in improved damping characteristics. To improve the performance of the piezoelectric materials to control the vibrations of structures, they are employed as constraining layer of the ACLD treatment rather than directly attached to the host structures. Further, the ACLD treatment works as a passive constrained layer damping (PCLD) treatment in the absence of applied voltages. Thus, the ACLD treatment provides both passive and active damping simultaneously when under operation [26,27]. In recent decades, a great deal of work has been carried out on demonstration of the effectiveness of ACLD treatment for attenuating the vibrations of light-weight flexible structures [28–35]. Ray et al. [34] experimentally and theoretically analyzed the ACLD of the cylindrical shell. Datta and Ray [36] developed a three-dimensional fractional derivative model for active constrained layer damping of composite plates. Kundalwal and Ray [37] investigated the smart damping of fuzzy fiber-reinforced composite plates using ACLD. Lim et al. [38] developed the closed loop finite element modeling of ACLD for time domain analysis.

In this paper, geometrically nonlinear vibration control of multiferroic fibrous composite plate i.e., piezoelectric ($BaTiO_3$) fiber reinforced magneto-electro-elastic (FRMEE) plate using the constrained layer damping has been investigated. The constrained viscoelastic layer of the ACLD treatment is modeled by using Golla–Hughes–McTavish (GHM) method in time domain. Incorporating the von Kármán type nonlinear strain-displacement relations and layer-wise shear deformation theory, a three-dimensional finite element (FE) model of the overall FRMEE plate integrated with the ACLD patches has been developed. The influence of electro-elastic, magneto-elastic and electromagnetic coupled fields on the vibration has been studied. Furthermore, effects of various parameters such as the effect of piezoelectric fiber volume fraction (V_f), fiber orientation angle in the substrate, variation of the piezoelectric fiber orientation in the 1–3 PZC constraining layer and the boundary conditions on the control of geometrically nonlinear vibrations of the multiferroic fibrous plate or FRMEE plates has been investigated.

2. Problem description

A schematic diagram of multilayred FRMEE composite plate integrated with a patch of the ACLD treatment on its top surface is illustrated in Fig. 1(a) while Fig. 1(b) illustrates a layer of the FRMEE plate. Although one patch is shown in Fig. 1(a), the FE model is derived for a multiple number of patches. The length, the width and the total thickness of the FRMEE plate are *a*, *b* and *H*, respectively. The thickness of the constraining PZC layer and the constrained viscoelastic layer of the ACLD treatment are h_p and h_v, respectively. Each layer of the FRMEE plate composed of the piezoelectric fibers embedded within the piezomagnetic matrix. The effective material properties of the FRMEE composites with different fiber volume fractions have been considered from the open literature [17]. Since both the piezoelectric and the piezomagnetic constituents are present in each layer of the FRMEE plate, hence all layers of the FRMEE plate exhibit the piezoelectric and piezomagnetic effects unlike the MEE plates studied by Kattimani and Ray [10] wherein the individual layers exhibit either piezoelectric or magnetostrictive effect.

2.1. Kinematics of deformations

The kinematics of deformations of the undeformed transverse normal in the *xz*- and the *yz*-planes are illustrated in Fig. 2 (a) and (b), respectively. The thicknesses of the substrate plate, substrate layer, piezoelectric layer and viscoelastic layer are represented by H, h, h_p and h_v, respectively. The rotations of the portions of the normal lying in the substrate plate, the viscoelastic layer, and the piezoelectric layer are represented by θ_x, ϕ_x and γ_x, respectively in the *xz*-plane, while θ_y, ϕ_y and γ_y

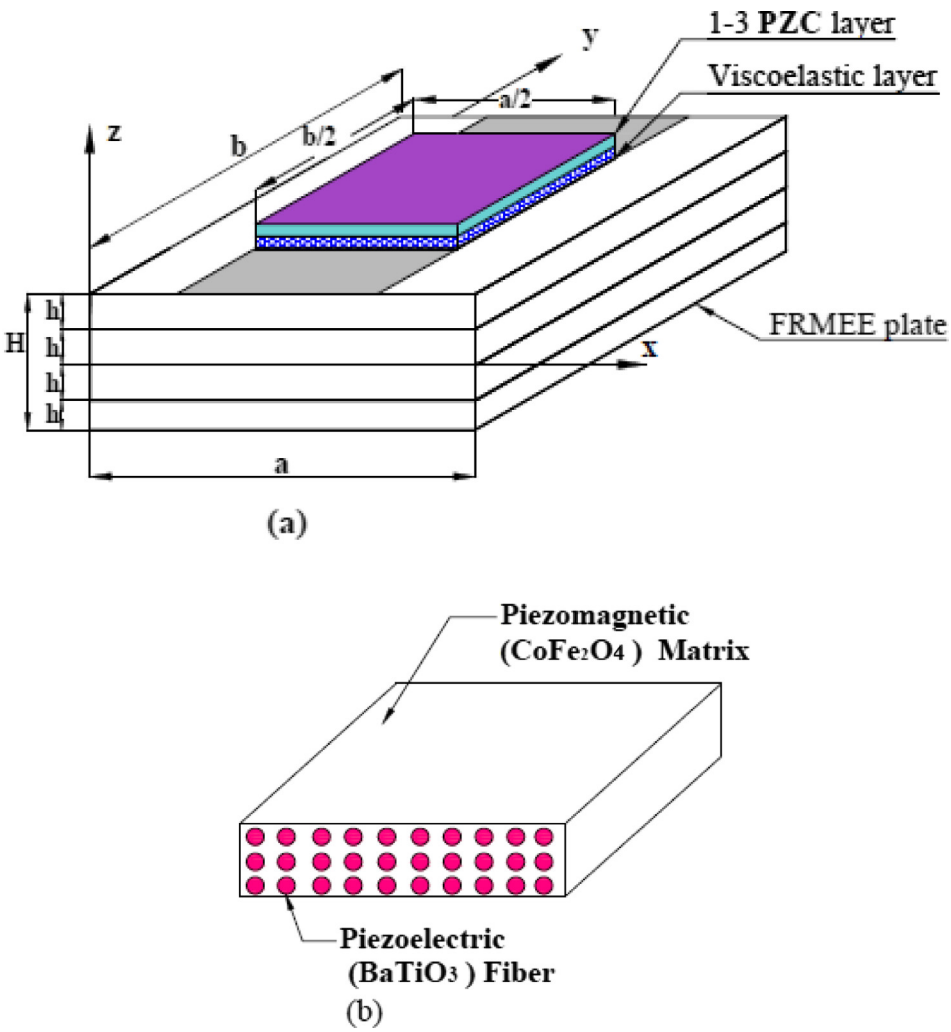

Fig. 1. (a) Schematic representation of a FRMEE plate (b) layer of FRMEE plate.

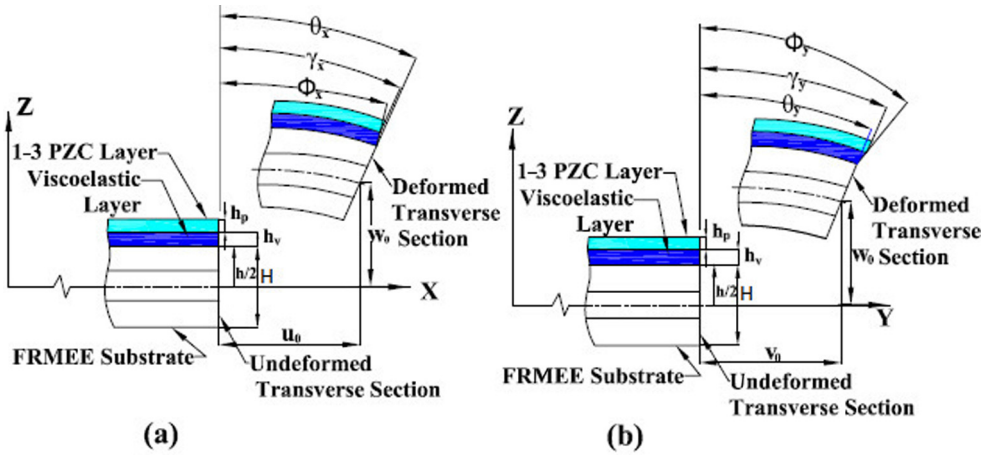

Fig. 2. Kinematics of deformations of the FRMEE plate integrated with the ACLD patch (a) Transverse cross section parallel to *xz*-plane, (b) transverse cross section parallel to *yz*-plane.

represent the same in the *yz*-plane. Consequently, the axial displacements u and v of any point in the overall plate along the x- and y-directions, respectively, can be written as:

$$u(x,y,t) = u_0(x,y,t) + \beta_1(z)\theta_x(x,y,t) + \beta_2(z)\phi_x(x,y,t) + \beta_3(z)\gamma_x(x,y,t) \tag{1a}$$

$$v(x,y,t) = v_0(x,y,t) + \beta_1(z)\theta_y(x,y,t) + \beta_2(z)\phi_y(x,y,t) + \beta_3(z)\gamma_y(x,y,t) \tag{1b}$$

where $\beta_1(z) = z - \langle z - h/2\rangle$, $\beta_2(z) = \langle z - h/2\rangle - \langle z - h_{N+1}\rangle$ and $\beta_3(z) = \langle z - h/2\rangle - \langle z - h_{N+2}\rangle$.

It may be noted that the overall composite plate consists of different continua consisting of the substrate piezoelectric and magnetostrictive material, viscoelastic material and the constraining PZC material. Consequently, to ensure the continuity of the displacement field at the interface between the viscoelastic layer and the PZC layer or between the substrate plate and the viscoelastic layer, the appropriate singularity functions $\beta_1(z)$, $\beta_2(z)$ and $\beta_3(z)$ are defined in Eq. (1). In order to utilize the vertical actuation by the active constraining layer of the ACLD treatment and to achieve the accurate results, a higher order transverse deformation theory has been assumed for the overall plate. Accordingly, the transverse displacement at any point in the overall plate can be expressed as

$$w(x,y,z,t) = w_0(x,y,t) + z\theta_z(x,y,t) + z^2\phi_z(x,y,t) \tag{2}$$

In Eqs. (1) and (2), variables u_0, v_0 and w_0 are the translational displacements at any point on the mid-plane (z = 0) of the substrate along x-, y- and z-directions, respectively, with θ_z and ϕ_z are the generalized rotational displacements. To facilitate the computation, the rotational variables $\{d_r\}$ are separated from the translational displacement variables $\{d_t\}$ as follows:

$$\{d_t\} = \begin{bmatrix} u_0 & v_0 & w_0 \end{bmatrix}^T \text{ and } \{d_r\} = \begin{bmatrix} \theta_x & \theta_y & \theta_z & \phi_x & \phi_y & \phi_z & \gamma_x & \gamma_y \end{bmatrix}^T \tag{3}$$

2.2. Strain-displacement relations

Since the FRMEE plate integrated with ACLD patches is a thin structure, the shear locking problems should be alleviated by employing the selective integration rule in a straightforward manner. To facilitate this task, the state of strain at any point in the overall FRMEE plate is expressed by the strain vector $\{\varepsilon_b\}$ containing in-plane strains and transverse normal strain and the vector $\{\varepsilon_s\}$ of transverse shear strains as follows:

$$\{\varepsilon_b\} = \{\, \varepsilon_x \quad \varepsilon_y \quad \varepsilon_z \quad \varepsilon_{xy} \,\} \text{ and } \{\varepsilon_s\} = \{\, \varepsilon_{xz} \quad \varepsilon_{yz} \,\} \tag{4}$$

in which, ε_x, ε_y, and ε_z are the normal strains along x-, y- and z- directions, respectively; ε_{xy} is the in-plane shear strain, ε_{xz} and ε_{yz} are the transverse shear strains. Employing the von Kármán type geometrically nonlinear strain-displacement relations the strain vectors $\{\varepsilon_b^k\}$ representing the state of in-plane and transverse normal strains at any point in the FRMEE plate, the viscoelastic layer and the piezoelectric actuator layer, respectively, can be stated as:

$$\{\varepsilon_b^k\} = \{\varepsilon_{bt}\} + [Z_1]\{\varepsilon_{rb}\} + \{\varepsilon_{tbn}\}; \quad k = 1,2,3,\ldots,N$$

$$\{\varepsilon_b^k\} = \{\varepsilon_{bt}\} + [Z_2]\{\varepsilon_{rb}\} + \{\varepsilon_{tbn}\}; \quad k = N+2 \tag{5}$$

Here, k designates the layer number starting from the bottom layer of the overall plate. Analogously, the strain vectors representing the state of transverse shear strains at any point in the substrate, the viscoelastic layer, and the piezoelectric actuator layer, respectively, can be stated as follows:

$$\{\varepsilon_s^k\} = \{\varepsilon_{ts}\} + [Z_3]\{\varepsilon_{rs}\};\ \mathrm{k} = 1,2,3.,\ldots,\mathrm{N} \quad \{\varepsilon_s^k\} = \{\varepsilon_{ts}\} + [Z_4]\{\varepsilon_{rs}\};\ \mathrm{k} = \mathrm{N}+1 \text{ and}$$

$$\{\varepsilon_s^k\} = \{\varepsilon_{ts}\} + [Z_5]\{\varepsilon_{rs}\}; \quad \mathrm{k} = \mathrm{N}+2 \tag{6}$$

The transformation matrices [Z_1] - [Z_5], the generalized strain vectors ($\{\varepsilon_{bt}\}$, $\{\varepsilon_{ts}\}$, $\{\varepsilon_{rb}\}$, $\{\varepsilon_{rs}\}$) and the generalized nonlinear strain vector ($\{\varepsilon_{tbn}\}$) appearing in Eqs. (5) and (6) are presented in the Appendix A. Analogous to the representation of the state of strains given in Eq. (5), the state of stress at any point in the overall FRMEE plate can be written as follows:

$$\{\sigma_b\} = [\,\sigma_x \quad \sigma_y \quad \sigma_z \quad \sigma_{xy}\,]^T \text{ and } \{\sigma_s\} = [\,\sigma_{xz} \quad \sigma_{yz}\,]^T \tag{7}$$

in which σ_x, σ_y and σ_z are the normal stresses along x-, y- and z-directions, respectively; σ_{xy} is the in-plane shear stress; σ_{xz} and σ_{yz} are the transverse shear stresses.

2.3. Constitutive relations

The applied electric and magnetic fields are considered to act along the z-direction only. Thus the coupled constitutive relations for FRMEE layers with respect to the principal material coordinate axes are given by

$$\{\sigma_b^k\} = [\bar{C}_b^k]\{\varepsilon_b^k\} - \{e_b^k\}E_z - \{q_b^k\}H_z \text{ and } \{\sigma_s^k\} = [\bar{C}_s^k]\{\varepsilon_s^k\}$$

$$D_z = \{e_b^k\}^T\{\varepsilon_b^k\} + \in_{33}^k E_z + d_{33}H_z$$

$$B_z = \{q_b^k\}^T\{\varepsilon_b^k\} + d_{33}E_z + \mu_{33}H_z \quad \mathrm{k} = 1,2,3 \tag{8}$$

where k = 1, 2, 3,. .., N, D_z and B_z are the electric displacement and the magnetic induction (i.e., magnetic flux), respectively, along the z-direction; E_z and H_z are the electrical field and the magnetic field, respectively, along the z-direction; $[\bar{C}_b^k]$ and $[\bar{C}_s^k]$ are the transformed elastic coefficient matrix; $\in_{33}^k$ and μ_{33} are the dielectric constant and the magnetic permeability constant, respectively; $\{e_b^k\}$, $\{q_b^k\}$ and d_{33} are the piezoelectric coefficient matrix, the magnetostrictive coefficient matrix, and the electromagnetic coefficient, respectively. The various matrices of material properties appearing in Eq. (8) are given by

$$[\bar{C}_b^k] = \begin{bmatrix} C_{11}^k & C_{12}^k & C_{13}^k & 0 \\ C_{12}^k & C_{22}^k & C_{23}^k & 0 \\ C_{13}^k & C_{32}^k & C_{33}^k & 0 \\ 0 & 0 & 0 & C_{66}^k \end{bmatrix},\ [\bar{C}_s^k] = \begin{bmatrix} C_{55}^k & 0 \\ 0 & C_{66}^k \end{bmatrix},\ \{e_b^k\} = \begin{Bmatrix} e_{31} \\ e_{32} \\ e_{33} \\ e_{36} \end{Bmatrix},\ \{q_b^k\} = \begin{Bmatrix} q_{31} \\ q_{32} \\ q_{33} \\ q_{36} \end{Bmatrix} \tag{9}$$

while with respect to the laminate coordinate system, the elastic coefficient matrices $[\bar{C}_b^k]$ and $[\bar{C}_s^k]$, the piezoelectric coefficient vector $\{e^k\}$, the dielectric coefficient vector $\{\varepsilon^k\}$ and the magnetic coefficient vector $\{q^k\}$ of the off-axis FRMEE lamina are to be augmented as follows:

$$[\bar{C}_b^k] = \begin{bmatrix} \bar{C}_{11}^k & \bar{C}_{12}^k & \bar{C}_{13}^k & \bar{C}_{16}^k \\ \bar{C}_{12}^k & \bar{C}_{22}^k & \bar{C}_{23}^k & \bar{C}_{26}^k \\ \bar{C}_{13}^k & \bar{C}_{32}^k & \bar{C}_{33}^k & \bar{C}_{36}^k \\ \bar{C}_{16}^k & \bar{C}_{26}^k & \bar{C}_{36}^k & \bar{C}_{66}^k \end{bmatrix},\ [\bar{C}_s^k] = \begin{bmatrix} \bar{C}_{55}^k & \bar{C}_{45}^k \\ \bar{C}_{45}^k & \bar{C}_{66}^k \end{bmatrix},$$

$$\{\bar{e}_b^k\} = \{\,\bar{e}_{31} \quad \bar{e}_{32} \quad \bar{e}_{33} \quad \bar{e}_{36}\,\},\ \{\bar{\varepsilon}_b^k\} = \{\varepsilon_{33}\} \text{ and}$$

$$\{\bar{q}_b^k\} = \{\,\bar{q}_{31} \quad \bar{q}_{32} \quad \bar{q}_{33} \quad \bar{q}_{36}\,\} \tag{10}$$

The constitutive relations for the 1–3 PZC constraining layer of the ACLD treatment adaptable with the present method of finite element formulation are given by

$$\{\sigma_b^k\} = [\bar{C}_b^k]\{\varepsilon_b^k\} - [\bar{C}_{bs}]\{\varepsilon_s^k\} - \{\bar{e}_b\}E_z,$$

$$\{\sigma_s^k\} = [\bar{C}_{bs}]^T\{\varepsilon_b^k\} + [\bar{C}_s^k]\{\varepsilon_s^k\} - \{\bar{e}_b\}E_z \text{ and}$$

$$D_z = \{\bar{e}_b\}^T\{\varepsilon_b^k\} + \{\bar{e}_s\}^T\{\varepsilon_s^k\} + \bar{\in}_{33}E_z \quad (\mathrm{k} = 5) \tag{11}$$

In Eq. (11), the forms of the transformed elastic coefficient matrices $[\bar{C}_b^k]$ and $[\bar{C}_s^k]$ are similar to those of $[\bar{C}_b^k]$ and $[\bar{C}_s^k]$, respectively. However, the constitutive relations reveal that the inclination of the piezoelectric fibers in the vertical *xz*- or *yz*-plane is responsible for the coupling between the transverse shear strains and the in-plane stresses. The corresponding coupling elastic constant matrix $[\bar{C}_{bs}^5]$ is given by

$$[\bar{C}_{bs}^5] = \begin{bmatrix} \bar{C}_{15} & \bar{C}_{25} & \bar{C}_{35} & 0 \\ 0 & 0 & 0 & \bar{C}_{46} \end{bmatrix}^T \text{ or } [\bar{C}_{bs}^5] = \begin{bmatrix} 0 & 0 & \bar{C}_{56} & 0 \\ \bar{C}_{14} & \bar{C}_{24} & 0 & \bar{C}_{34} \end{bmatrix}^T \tag{12}$$

according to as the fibers are coplanar with the *xz*- or the *yz*-plane, respectively. If the piezoelectric fibers are coplanar with both the *xz*- and the *yz*-planes ($\lambda = 0$), the coupling matrix of Eq. (12) transforms into a null matrix. Also, the piezoelectric constant matrices $\{e_b^k\}$ and $\{e_s^k\}$ appearing in Eq. (12) involve the following transformed effective piezoelectric coefficients of the 1–3 PZC:

$$\{\bar{e}_b\} = \{\, \bar{e}_{31} \quad \bar{e}_{32} \quad \bar{e}_{33} \quad \bar{e}_{36} \,\}^T \text{ and } \{\bar{e}_s\} = \{\, \bar{e}_{35} \quad \bar{e}_{34} \,\}^T \tag{13}$$

The present analysis of the overall MEE plates will be carried out in the time domain. Consequently, the Golla–Hughes–McTavish (GHM) method has been implemented to model the viscoelastic material. For time domain analysis, the constitutive equation for the linear, isotropic and homogeneous viscoelastic material is expressed in stieltjes integral form and is given by

$$(\sigma_s)_v = \int_0^t G(t-\tau)\frac{\partial(\varepsilon_s^k)}{\partial\tau}d\tau, \quad \mathrm{k} = 4 \tag{14}$$

where G(t) is the relaxation function of the viscoelastic material.

2.4. Electric field-potential relations

Using Maxwell's electromagnetic equations, the transverse electric and magnetic fields are considered for deriving the FE model. It is also to be noted that the transverse magnetoelastic and piezoelectric constants for all the FRMEE layers are equal. Hence, same functions for the distribution of the transverse electric field and the magnetic field are considered for deriving the model. Thus the transverse electric field and the transverse magnetic field in any FRMEE lamina can be related to the electric potential and the magnetic potential, respectively as follows:

$$E_z = -\frac{\partial\phi}{\partial z} \text{ and } \quad H_z = -\frac{\partial\psi}{\partial z} \tag{15}$$

in which E_z, H_z, ϕ and ψ are the transverse electric field, the transverse magnetic field, the electrical potential function, and the magnetic potential function, respectively. The electric and the magnetic potential functions can be written as

$$\phi = \frac{z-h_1}{H}\bar{\phi} \text{ and } \quad \psi = \frac{z-h_1}{H}\bar{\psi} \tag{16}$$

in which, H is the total thickness of the substrate, h_1 is the z-coordinate of the bottom surface of the bottom layer of the substrate.

3. Finite element model of FRMEE plate integrated with ACLD patches

Considering that the FRMEE plate is composed of N number of FRMEE layers of different fiber orientation angles, the principle of virtual work employed to derive the governing equations of the overall FRMEE plate is given by

$$\begin{aligned} &\sum_{k=1}^{N+2}\int_{\Omega^k}\delta\{\varepsilon_b^k\}^T\{\sigma_b^k\}d\Omega^k + \sum_{k=1}^{n+2}\int_{\Omega^k}\delta\{\varepsilon_s^k\}^T\{\sigma_s^k\}d\Omega^k + \int_{\Omega^5}\left(\delta\{\varepsilon_b^5\}^T\{\sigma_b^5\} + \delta\{\varepsilon_s^5\}^T\{\sigma_s^5\}\right)d\Omega^5 \\ &- \int_{\Omega^{N+2}}\delta E_z^{N+2}D_Z^{N+2}d\Omega^{N+2} - \int_{\Omega^k}\delta E_z D_z d\Omega - \int_{\Omega^k}\delta H_z B_z d\Omega - \int_A \delta\{d_t\}^T\{f\}dA \\ &+ \sum_{k=1}^{N+2}\int_{\Omega^k}\delta\{d_t\}^T\rho^k\{\ddot{d}_t\}d\Omega^t = 0 \end{aligned} \tag{17}$$

where ρ^k is the mass density of the kth layer, Ω^k (k = 1, 2, 3, …, 5) indicates the volume of the relevant layer, $\{f\} = [0\ 0\ p]^T$ is the externally applied surface traction vector acting over a surface area A with p being the transverse step load and δ is the symbol of the first variation. The overall FRMEE plate integrated with the ACLD patch is discretized by eight noded isoparametric quadrilateral elements. The generalized displacement vectors $\{d_{ti}\}$ and $\{d_{ri}\}$ associated with the ith (i = 1, 2, 3, …, 8) node of the element can be written as

$$\{d_{ti}\} = [\, u_{0i} \quad v_{0i} \quad w_{0i} \,]^T \text{ and } \{d_{ri}\} = \left[\, \theta_{xi} \quad \theta_{yi} \quad \theta_{zi} \quad \phi_{xi} \quad \phi_{yi} \quad \phi_{zi} \quad \gamma_{xi} \quad \gamma_{yi} \,\right]^T \tag{18}$$

while the electric potential vector $\{\phi\}$ and the magnetic potential $\bar{\psi}$ at any point within the element can be expressed in terms of the nodal electric potential vector $\{\phi^e\}$ and the nodal magnetic potential vector $\{\bar{\psi}^e\}$, respectively, as follows:

$$\{\phi\} = [N_\phi]\{\phi^e\} \text{ and } \bar{\psi} = [N_\psi]\{\bar{\psi}^e\} \tag{19}$$

in which,

$$\{\phi^e\} = [\,\phi_1 \quad \phi_2 \quad . \quad . \quad . \quad \phi_8\,]^T,\ \{\bar{\psi}^e\} = [\,\bar{\psi}_1 \quad \bar{\psi}_2 \quad . \quad . \quad . \quad \bar{\psi}_8\,]^T$$

$$[N_\phi] = [\,n_1 \quad n_2 \quad . \quad . \quad . \quad n_8\,]^T \text{ and } [N_\psi] = [N_\phi] \tag{20}$$

where n_i is the shape function of natural coordinates associated with the ith node, ϕ_i (i = 1, 2, 3,. . ., 8) are the nodal electric potential degrees of freedom and $\bar{\psi}_i$ (i = 1, 2, 3,. . ., 8) are the nodal magnetic potential degrees of freedom. $[N_\phi]$ and $[N_\psi]$ are the (3×24) shape function matrices. Using Eqs. (15), (16) and (19), the transverse electric field E_z and the transverse magnetic field H_z can be expressed as

$$E_z = -\frac{1}{H}[N_\phi]\{\phi^e\} \text{ and } H_z = -\frac{1}{H}[N_\psi]\{\bar{\psi}^e\} \tag{21}$$

Now, using Eqs. (5), (6) and (21), the strain vectors at any point within the element can be expressed in terms of the nodal generalized displacement vectors as follows:

$$\{\varepsilon_{bt}\} = [B_{tb}]\{d_t^e\}, \quad \{\varepsilon_{br}\} = [B_{rb}]\{d_r^e\}, \quad \{\varepsilon_{tbn}\} = \frac{1}{2}[B_1][B_2]\{d_t^e\},$$

$$\{\varepsilon_{st}\} = [B_{ts}]\{d_t^e\} \text{ and } \{\varepsilon_{rs}\} = [B_{rs}]\{d_r^e\} \tag{22}$$

in which the nodal strain-displacement matrices $[B_{tb}]$, $[B_{rb}]$, $[B_{ts}]$, $[B_{rs}]$, $[B_1]$ and $[B_2]$ are explicitly presented in the Appendix A. Now, by substituting Eqs. (5), (6), (10), (21) and (22) into Eq. (17), the elemental equations of motion for the FRMEE plate integrated with the ACLD treatment obtained are presented explicitly in Appendix B. The elemental equations of motion are assembled in a straightforward manner into the global space to obtain the open-loop coupled global equations of motion of the overall smart FRMEE plate integrated with the patches of the ACLD treatment as follows:

$$[M]\{\ddot{X}\} + [K_{tt}]\{X\} + [K_{tr}]\{X_r\} + [K_{t\phi}]\{\Phi\} + [K_{t\psi}]\{\psi\} + [K_{tsv}]\int_0^t G(t-\tau)\frac{\partial}{\partial\tau}\{X\}d\tau + [K_{trsv}]\int_0^t G(t-\tau)\frac{\partial}{\partial\tau}\{X_r\}d\tau$$
$$= \{F\} - \sum_{j=1}^{q}(\{F_{tp}^j\} + \{F_{tpn}^j\})V^j \tag{23}$$

$$[K_{tr}]^T\{X\} + [K_{rr}]\{X_r\} + [K_{trsv}]^T\int_0^t G(t-\tau)\frac{\partial}{\partial\tau}\{X\}d\tau + [K_{rrsv}]\int_0^t G(t-\tau)\frac{\partial}{\partial\tau}\{X_r\}d\tau + [K_{r\phi}]\{\Phi\} + [K_{r\psi}]\{\psi\}$$
$$= -\sum_{j=1}^{q}\{F_{rp}^j\}V^j \tag{24}$$

$$[K_{t\phi}]^T\{X\} + [K_{r\phi}]^T\{X_r\} - [K_{\phi\phi}]\{\Phi\} = 0 \tag{25}$$

$$[K_{t\psi}]^T\{X\} + [K_{r\psi}]^T\{X_r\} - [K_{\psi\psi}]\{\psi\} = 0 \tag{26}$$

where [M] is the global mass matrix; $[K_{tt}]$, $[K_{tr}]$, $[K_{rr}]$ $[K_{tsv}]$, $[K_{trsv}]$ and $[K_{trsv}]$ are the global elastic stiffness matrices, $[K_{t\phi}]$ and $[K_{r\phi}]$ are the global electro-elastic coupling stiffness matrices, $[K_{t\psi}]$ and $[K_{r\psi}]$ are the global magneto-elastic coupling stiffness matrices, $[K_{\phi\phi}]$ is the global electrical stiffness matrix, $[K_{\psi\psi}]$ is the global magnetic stiffness matrix, $\{F_{tp}\}$ and $\{F_{rp}\}$ are the global electro-elastic coupling vectors; $\{F\}$ is the global nodal mechanical load vector, respectively, $\{X\}$ and $\{X_r\}$ are the global generalized nodal displacement vectors, $\{\Phi\}$ and $\{\psi\}$ are the global nodal generalized electrical potential and magnetic potential vectors, $\mathbf{V^j}$ is the applied control voltage to the jth ACLD patch. In the absence of the applied control voltage, the coupled global equations derived above also govern the passive (uncontrolled) constrained layer damping of the MEE plate. After standard condensation of $\{\Phi\}$ and $\{\boldsymbol{\psi}\}$, invoking the boundary conditions and taking the Laplace transform of Eqs. (23) and (24), the following global equations in the Laplace domain are obtained:

$$s^2[M]\{\tilde{X}_t\} + L([K_1]\{X_t\} + [K_2]\{X_r\}) + [K_{tsv}]s\tilde{G}(s)\{\tilde{X}_t\} + [K_{trsv}]s\tilde{G}(s)\{\tilde{X}_r\} = \{\tilde{F}\} - \sum_{j=1}^{q}\{F_{tp}^j\}\tilde{V}^j - L\left(\sum_{j=1}^{q}\{F_{tpn}^j\}V^j\right) \tag{27}$$

$$L([K_3]\{X_t\}) + [K_4]\{\tilde{X}_r\} + [K_{trsv}]^T s\tilde{G}(s)\{\tilde{X}_t\} + [K_{rrsv}]s\tilde{G}(s)\{\tilde{X}_r\} = -\sum_{j=1}^{q}\{F_{rp}^j\}\tilde{V}^j \tag{28}$$

in which, the augmented matrices are given by

$$[K_1] = [K_{tt}] + [K_{t\phi}][K_{\phi\phi}]^{-1}[K_{t\phi}]^T + [K_{t\psi}][K_{\psi\psi}]^{-1}[K_{t\psi}]^T,$$

$$[K_2] = [K_{tr}] + [K_{t\phi}][K_{\phi\phi}]^{-1}[K_{r\phi}]^T + [K_{r\psi}][K_{\psi\psi}]^{-1}[K_{r\psi}]^T,$$

$$[K_3] = [K_{rt}] + [K_{r\phi}][K_{\phi\phi}]^{-1}[K_{\phi t}]^T + [K_{r\psi}][K_{\psi\psi}]^{-1}[K_{\psi t}]^T,$$

$$[K_4] = [K_{rr}] + [K_{r\phi}][K_{\phi\phi}]^{-1}[K_{r\phi}]^T + [K_{r\psi}][K_{\psi\psi}]^{-1}[K_{r\psi}]^T \tag{29}$$

where L is the Laplace operator while $\{\tilde{X}_t\}$, $\{\tilde{X}_r\}$, $\{\tilde{F}\}$ and $\tilde{V}^j$ are Laplace transforms of $\{X_t\}$, $\{X_r\}$, {F} and V^j, respectively.

3.1. Implementation of the GHM method

Although, the implementation of the GHM method in time domain is analogous to one studied by Kattimani and Ray [10] for the MEE plate, for the sake of clarity the method is presented here again. Using the GHM model for the viscoelastic material in time domain, the material modulus function can be expressed by a series of mini-oscillator terms [40] as follows:

$$s\tilde{G}(s) = G^{\infty}\left[1 + \sum_{k=1}^{N}\alpha_k \frac{s^2 + 2\hat{\xi}_k\hat{\omega}_k s}{s^2 + 2\hat{\xi}_k\hat{\omega}_k s + \hat{\omega}_k^2}\right] \tag{30}$$

in which, the term $s\tilde{G}(s)$ is referred to as a material modulus function of the viscoelastic material in the Laplace domain. G^{∞} is the equilibrium value of the modulus i.e. the final value of the relaxation G(t). Every mini-oscillator term is a second-order rational function consisting of three positive constants α_k, $\hat{\omega}_k$ and $\hat{\xi}_k$. These constants influence the shape of the modulus function in the complex s-domain. Taking into consideration of a GHM material modulus function with a single mini-oscillator term [40] i.e.,

$$s\tilde{G}(s) = G^{\infty}\left[1 + \alpha \frac{s^2 + 2\hat{\xi}\hat{\omega}s}{s^2 + 2\hat{\xi}\hat{\omega}s + \hat{\omega}^2}\right] \tag{31}$$

the auxiliary dissipation coordinates Z and Z_r are introduced as follows [46]:

$$s\tilde{G}(s)\{\tilde{X}_t\} = G^{\infty}[(1+\alpha)\{\tilde{X}_t\} - \alpha\tilde{Z}(s)] \text{ and } s\tilde{G}(s)\{\tilde{X}_r\} = G^{\infty}[(1+\alpha)\{\tilde{X}_r\} - \alpha\tilde{Z}_r(s)] \tag{32}$$

$$\tilde{Z}(s) = \frac{\hat{\omega}^2}{s^2 + 2\hat{\xi}\hat{\omega}s + \hat{\omega}^2}\{X_t\} \text{ and } \tilde{Z}_r(s) = \frac{\hat{\omega}^2}{s^2 + 2\hat{\xi}\hat{\omega}s + \hat{\omega}^2}\{X_r\} \tag{33}$$

where $\tilde{Z}(s)$ and $\tilde{Z}_r(s)$ are the Laplace transforms of Z and Z_r, respectively. Using Eqs. (31) and (32) in Eqs. (27) and (28), it can be written that

$$\begin{aligned} &s^2[M]\{\tilde{X}_t\} + L([K_1]\{X_t\} + [K_2]\{X_r\}) + G^{\infty}[K_{tsv}][(1+\alpha)\{\tilde{X}_t\} - \alpha\tilde{z}(s)] + G^{\infty}[K_{trsv}][(1+\alpha)\{\tilde{X}_r\} - \alpha\tilde{z}_r(s)] \\ &\quad = \{\tilde{F}\} - \sum_{j=1}^{q}\{F_{tp}^j\}\tilde{V}^j - L\left(\sum_{j=1}^{q}\{F_{tpn}^j\}V^j\right) \end{aligned} \tag{34}$$

$$L([K_3]\{X_t\}) + [K_4]\{\tilde{X}_r\} + [K_{trsv}]^T s\tilde{G}(s)\{\tilde{X}_t\} + [K_{rrsv}]s\tilde{G}(s)\{\tilde{X}_r\} = -\sum_{j=1}^{q}\{F_{rp}^j\}\tilde{V}^j \tag{35}$$

Taking inverse Laplace transforms of Eqs. (33)–(35) and condensing the global degrees of freedom $\{X_r\}$ from the resulting equations in time domain, the following equations are obtained:

$$[M]\{\ddot{X}_t\} + [K_x]\{X_t\} + [K_z]\{Z(t)\} + [K_{zr}]\{Z_r\} = \{F\} - \sum_{j=1}^{q}\{F_p^j\}V^j \tag{36}$$

$$\{\ddot{Z}\} + 2\xi\hat{\omega}\{\dot{Z}\} + \hat{\omega}^2\{Z\} - \hat{\omega}^2\{Z\} = 0 \tag{37}$$

$$\{\ddot{Z}_r\} + 2\xi\hat{\omega}\{\dot{Z}_r\} + \hat{\omega}^2[K_5]\{X_t\} - \hat{\omega}^2[K_6]\{Z\} - \hat{\omega}^2[K_7]\{Z_r\} = -\sum_{j=1}^{q}\{F_{pz}^j\}V^j \tag{38}$$

The various global stiffness matrices and force vectors appearing in Eqs. (36)–(38) given in Appendix. C. Now, Eqs. (36)–(38) are combined to obtain the global open-loop equations of motion in the time domain as follows:

$$[M^*]\{\ddot{X}\} + [C^*]\{\dot{X}\} + [K^*]\{X\} = \{F^*\} + \sum_{j=1}^{q}\{\bar{F}_p^j\}V^j \tag{39}$$

where

$$[M^*] = \begin{bmatrix} [M] & 0 & 0 \\ 0 & I_Z & 0 \\ 0 & 0 & I_{Z_r} \end{bmatrix}, \quad [C^*] = \begin{bmatrix} 0 & 0 & 0 \\ 0 & 2\xi\hat{\omega} & 0 \\ 0 & 0 & 2\xi\hat{\omega} \end{bmatrix}, \quad [K^*] = \begin{bmatrix} [K_x] & [K_z] & [K_{zr}] \\ -\hat{\omega}^2 & \hat{\omega}^2 & 0 \\ \hat{\omega}^2[K_5] & -\hat{\omega}^2[K_6] & \hat{\omega}^2[K_7] \end{bmatrix}$$

$$\{F^*\} = \begin{Bmatrix} \{F\} \\ 0 \\ 0 \end{Bmatrix}, \quad \{\bar{F}_p^j\} = \begin{Bmatrix} \{F_p^j\} \\ 0 \\ \{F_{pz}^j\} \end{Bmatrix}, \quad \{X\} = \begin{Bmatrix} \{X_t\} \\ Z \\ Z_r \end{Bmatrix} \tag{40}$$

4. Closed loop model

The control voltage V^j for activating the constraining layer of each ACLD patch is supplied according to a simple velocity feedback control law. Thus, the control voltage for each patch can be represented in terms of the derivatives of the global nodal degrees of freedom as follows:

$$V^j = -K_d\dot{w}_0(x_j, y_j) = -K_d[U_t^j]\{\dot{X}\} \tag{41}$$

where K_d is the control gain for the jth ACLD patch and $[U_t^j]$ is the unit vector for expressing the transverse velocity of a point (x_j, y_j) in terms of the time derivative of the global nodal generalized translational displacements. Eventually, substituting Eq. (41) into Eq. (39), the final global equations of motion governing the closed-loop dynamics of the MEE plate integrated with the ACLD system can be obtained as follows:

$$[M^*]\{\ddot{X}\} + [C_d^*]\{\dot{X}\} + [K^*]\{X\} = \{F^*\} \tag{42}$$

in which, $[C_d^*]$ is the active damping matrix and is given by

$$[C_d^*] = [C^*] + \sum_{j=1}^{q} K_d\{\bar{F}_p^j\}[U_t^j] \tag{43}$$

5. Results and discussions

In this section, numerical results are presented to demonstrate the control of the geometrically nonlinear transient vibrations of the FRMEE plates using the ACLD treatment. The FE model derived in the preceding section is employed to derive the numerical results. The FRMEE plate considered for computing the numerical results is integrated either with a single ACLD patch at the center of the plate as shown in Fig. 1(a) or two identical patches placed at the opposite edges of the plate as shown by the shaded area in Fig. 1(a). The total volume of the two patches equals the volume of the single patch. Fig. 1 (b) illustrates the schematic diagram of a layer of FRMEE plate. A layer of the obliquely reinforced 1–3 PZC material in which

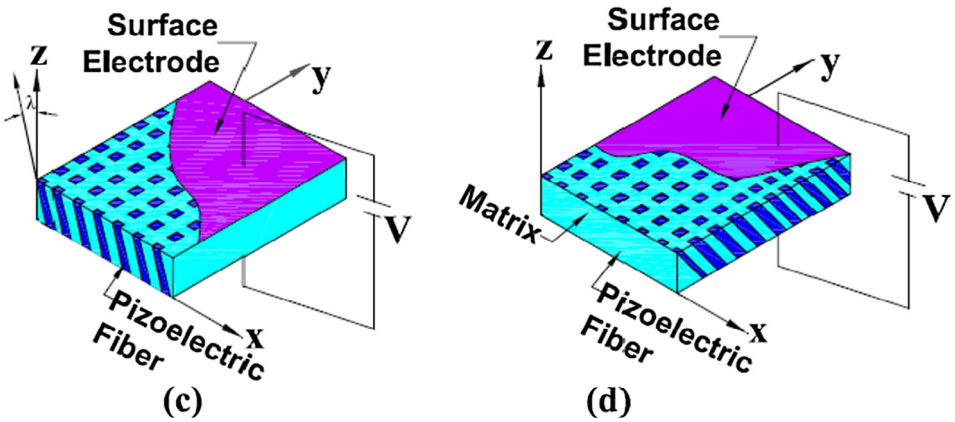

Fig. 3. Schematic representation of the ACLD patches with vertically/obliquely reinforced 1–3 PZCs in which (a) piezoelectric fibers are coplanar with the vertical *xz*-plane, (b) piezoelectric fibers are coplanar with the vertical *yz*-plane.

the piezoelectric fibers are coplanar with the *xz*-plane with their orientation angle λ with the z-axis is illustrated in Fig. 3(a). The piezoelectric fibers can be coplanar with the *yz*-plane while the orientation angle with the z-axis is λ as shown in Fig. 3 (b). In the case of the obliquely reinforced 1–3 PZC, the orientation angle (λ) is nonzero while it is zero for the vertically reinforced 1–3 PZC. The length and the width of the single ACLD patch are a/2 and b/2 while that of the patches placed on the edges are a/2 and b/4, respectively. The material of the constraining layer of the ACLD treatment is PZT-5H/spur epoxy composite with 60% piezoelectric fiber volume fraction. The elastic and the piezoelectric properties of this constraining 1–3 PZC layer are as follows [28]:

$$C_{11}^{P} = 9.29\ \text{GPa}, \quad C_{12}^{P} = 6.18\ \text{GPa}, \quad C_{13}^{P} = 6.05\ \text{GPa}, \quad C_{33}^{P} = 35.44\ \text{GPa}, \quad C_{23}^{P} = C_{13}^{P}$$

$$C_{44}^{P} = 1.58\ \text{GPa}, \quad C_{55}^{P} = 1.54\ \text{GPa}, \quad e_{31} = -0.1902 C/m^2, \quad e_{33} = 18.4107 C/m^2$$

The thicknesses of the constraining 1–3 PZC layer and the viscoelastic layer are considered to be 250 μm and 250 μm, respectively. Unless otherwise stated, the aspect ratio (*a/H*) of the FRMEE plate is considered to be 200 and the controlled responses are computed using the vertically reinforced 1–3 PZC (i.e. λ = 0°). The substrate plate is modeled by N layers of equal thickness (*h* = 0.001 m). The material properties of the substrate FRMEE plate for different volume fractions ($BaTiO_3$/$CoFe_2O_4$) are given in Table 1 [3,17]. In order to consider single term GHM expression, the values of α, $\hat{\xi}$ and $\hat{\omega}$ are used as 11.42, 20 and 1.0261 × 105, respectively [40]. The shear modulus (G^{∞}) and the density of the viscoelastic material (ρ_v) are used as 1.822 × 106 Pa and 1140 kg/m^3, respectively [40]. The boundary conditions employed for computing the numerical results are given in Table 2. In all cases, the electric and magnetic potentials at the boundaries are assumed to be zero. The open-loop and the closed-loop responses of the plates have been examined by the frequency response functions for the transverse displacement at the mid-point (a/2, b/2, H/2) of the substrate. A uniformly distributed transverse pulse load (p) is applied to set the overall plate into motion.

5.1. Validation of the GHM implementation

The implementation of the GHM method for modeling the ACLD treatment is validated with the methodology proposed by Lim et al. [38]. The viscoelastic material has been modeled by employing the conventional complex modulus approach and the GHM method separately to determine the linear frequency responses for the transverse displacement of the FRMEE plates. The first few modes of the FRMEE plate have been excited by applying a time-harmonic load of amplitude 1 N at the point (a/2, b/2, H/2). The frequency response functions obtained by the standard complex modulus approach as well as by the GHM method for the simply supported cross-ply (0°/90°/0°) FRMEE plate with 50% fiber volume fraction (V_f = 0.50) have been illustrated in Fig. 4. It may be observed from this figure that the frequency response curves obtained by both the approaches are almost indistinguishable. Consequently, it may be concluded that the present approach of modeling the viscoelastic material by the GHM method accurately evaluates the damping characteristics of the overall FRMEE plates in time domain.

Table 1
Material constants for FRMEE multiphase composites as percentage of piezoelectric [3,17].

Material properties with Units		25% $BaTiO_3$ (V_f = 0.25)	50% $BaTiO_3$ (V_f = 0.50)	75% $BaTiO_3$ (V_f = 0.75)
$C_{11} = C_{22}$	(10^9 N/m^2)	245	215	186
C_{12}	(10^9 N/m^2)	144	112	90
$C_{13} = C_{23}$	(10^9 N/m^2)	144	112	90
C_{33}	(10^9 N/m^2)	235	210	181
C_{44}	(10^9 N/m^2)	46	50	51
C_{66}	(10^9 N/m^2)	51	52	48
$e_{31} = e_{32}$	(C/m^2)	−1.5	−2.8	−3.8
e_{33}	(C/m^2)	4.2	8.7	13.2
$e_{24} = e_{15}$	(C/m^2)	0.0	0.2	0.3
$q_{31} = q_3$	(N/Am)	380	220	90
q_{33}	(N/Am)	475	290	135
$q_{24} = q_{15}$	(N/Am)	335	180	75
$\mu_{11} = \mu_{22}$	(10^{-6} Ns^2/C^2)	−3.55	−2.00	−0.90
μ_{33}	(10^{-6} Ns^2/C^2)	1.20	0.80	0.45
$\epsilon_{11} = \epsilon_{22}$	(10^{-9} C^2/Nm^2)	0.1	0.25	0.5
ϵ_{33}	(10^{-9} C^2/Nm^2)	3.2	6.3	9.4
d_{11}	(10^{-12} Ns/VC)	3.1	5.3	6.8
d_{33}	(10^{-12} Ns/VC)	2350	2750	1800
ρ	(kg/m^3)	5425	5550	5675

Table 2
Boundary conditions employed for the analysis of MEE plate.

Type	At $x = 0$ and a	At $y = 0$ and b
Simply Supported (SS1)	$v_0 = w_0 = \theta_y = \phi_y = \gamma_y = \theta_z = \phi_z = 0$	$u_0 = w_0 = \theta_x = \phi_x = \gamma_x = \theta_z = \phi_z = 0$
Clamped-Clamped (CC)	$u_0 = v_0 = w_0 = \theta_x = \theta_y = \phi_x = \phi_y = \gamma_y = \theta_z = \phi_z = 0$	$u_0 = v_0 = w_0 = \theta_x = \theta_y = \phi_x = \phi_y = \gamma_y = \theta_z = \phi_z = 0$

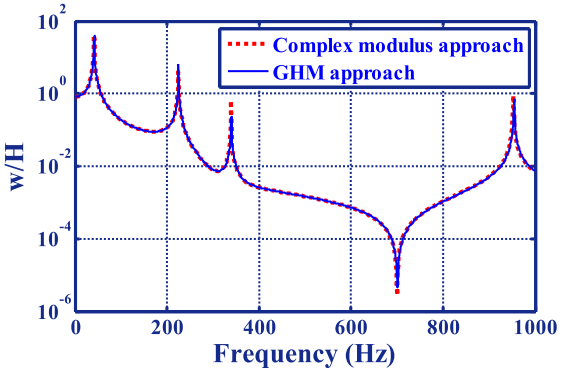

Fig. 4. Linear frequency responses for the center deflection of a simply supported symmetric cross-ply (0°/90°/0°) FRMEE plate obtained by the GHM method and the complex modulus approach.

5.2. Validation of the FE model

It is noteworthy to mention that to the authors' best knowledge, the research relevant to the geometrically nonlinear vibrations of the FRMEE plates is not yet reported in the open literature. However, the FRMEE layers can be replaced by the layers of the conventional composite. Hence, the load-deflection curve of the laminated composite plates presented by Sarangi and Ray [39] has been considered for the validation of the present FE model. Consequently, the variation of the non-dimensional vertical displacement w/H with respect to the load at the center of the cross-ply (0°/90°/0°) laminated plate integrated with the inactivated ACLD patches of negligible thickness has been computed by the present FE model and subsequently compared with the results reported by Sarangi and Ray [39] for the identical plate as shown in Fig. 5. It may be observed from this figure that the results are in excellent agreement.

5.3. Backbone curves and nonlinear dynamics

The open-loop and the closed-loop responses of the plates are examined by the frequency response functions for the transverse displacement at the mid-point (a/2, b/2, H/2) of the substrate. A uniformly distributed transverse step load (p) is applied to set the overall plate into motion. The magnitude of the exciting step load which causes the geometrically nonlinear deflections is determined by the backbone curves demonstrating the variations of the frequency ratio (ω_{nl}/ω_l) with the non-dimensional transverse deflection (w_{max}/H). Fig. 6 illustrates such backbone curves for a simply supported antisymmet-

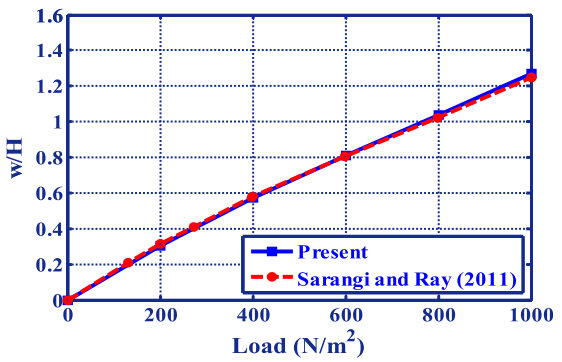

Fig. 5. Load deflection curves for a simply supported symmetric cross-ply (0°/90°/0°) square substrate plates.

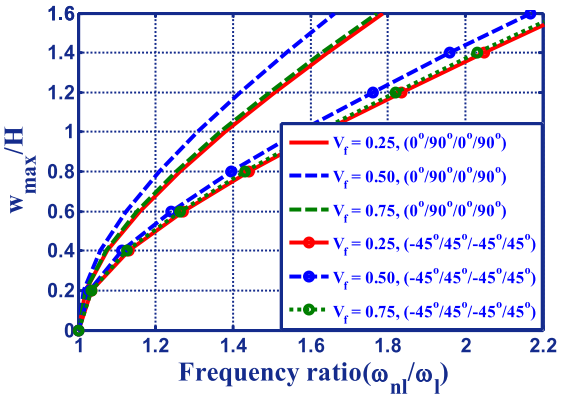

Fig. 6. Backbone curves for the simply supported antisymmetric cross-ply (0°/90°/0°/90°) and angle-ply (−45°/45°/−45°/45°) FRMEE plates for different volume fractions (V_f).

ric cross-ply (0°/90°/0°/90°) and antisymmetric angle-ply (−45°/45°/−45°/45°) FRMEE plates for different volume fractions (V_f). It may be noticed from these figures that for causing substantial geometrical nonlinearity ($\omega_{nl}/\omega_l > 1$) in the uncontrolled responses, the arbitrary applied step load should be such that the value of (w_{max}/H) is greater than 0.2.

5.4. Active damping analysis

The control voltage supplied to the ACLD patch is negatively proportional to the velocity of the point (a/2, b/2, H/2) on the top of the substrate. The values of the control gain (K_d) are chosen arbitrarily while maintaining the acceptable control voltage (V < 300 V). The nonlinear transient responses of a simply supported antisymmetric cross-ply (0°/90°/0°/90°) FRMEE plate with 50% volume fraction ($BaTiO_3/CoFe_2O_4$) is illustrated in Fig. 7 while Fig. 8 illustrates the same for the clamped-clamped antisymmetric cross-ply (0°/90°/0°/90°) FRMEE plate. The uncontrolled and controlled transient responses presented in these figures (Figs. 7 and 8) are corresponding to the cases when the patch is passive ($K_d = 0$) and active ($K_d \neq 0$), respectively. In both the cases, the plates are set into undergoing nonlinear vibrations with a same maximum amplitude of uncontrolled response ($K_d = 0$). It may be observed from these figures that the damping characteristics of the FRMEE plates have been substantially improved due to the active ACLD treatment and it has a significant effect on the control of geometrically nonlinear vibrations of the overall plates over the passive damping. Fig. 9 illustrates the corresponding control voltages required for the active control of responses presented in Figs. 7 and 8. It may be observed from this figure that the control voltages are within the nominal range (max (V) = 275 V).

Since the control voltage is proportional to the velocity of the center of the plate; the transient decay of the control voltage presented in Fig. 9 represents that the velocity at any point of the overall plate also diminishes with time. The phase plots illustrated in Fig. 10(a) and (b) for the simply supported and clamped-clamped boundary conditions, respectively, confirm the same demonstrating the stability of the plates. Figs. 11 and 12 illustrate the comparison of geometrically nonlinear transient vibration responses of simply supported symmetric cross-ply (0°/90°/0°) and antisymmetric angle-ply (−45°/45°/−45°/45°) FRMEE plates, respectively, with the piezoelectric ($BaTiO_3$) fiber volume fractions of 25%, 50% and 75% in the sub-

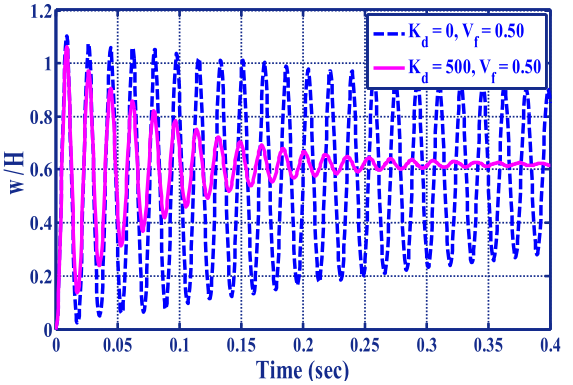

Fig. 7. Nonlinear transient responses of a simply supported antisymmetric cross-ply (0°/90°/0°/90°) FRMEE plate undergoing ACLD (a/H = 200, a = b, p = 1.8 kN/m^2).

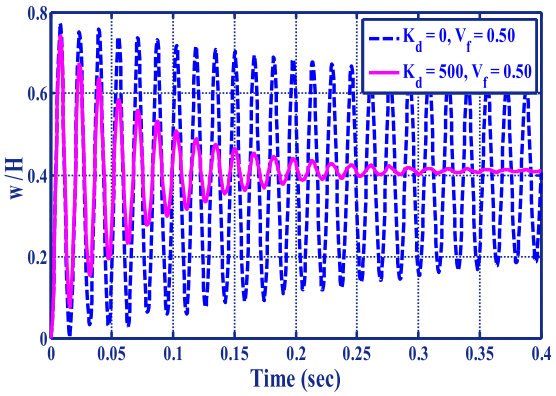

Fig. 8. Nonlinear transient responses of a clamped-clamped antisymmetric cross-ply (0°/90°/0°/90°) FRMEE plate undergoing ACLD (a/H = 200, a = b, p = 1.8 kN/m^2).

strate plate. It may be observed from these figures that the damping characteristic of the FRMEE plates increases with the decrease in the piezoelectric fiber volume fraction. Fig. 13 demonstrates the influence of lamination schemes on the nonlinear transient responses of simply supported FRMEE plates with 50% fiber volume fraction. It may be noticed from this figure that the antisymmetric angle-ply (−45°/45°/−45°/45°) FRMEE plate exhibits significantly higher stiffening effect than the antisymmetric cross-ply (0°/90°/0°/90°) FRMEE plates and the performance of the ACLD patch is significantly improved for attenuating the geometrically nonlinear vibrations. The transverse actuation by the 1–3 PZC layer of the ACLD patch mainly contributes significantly to enhancing the damping characteristics of the FRMEE plates as illustrated in Fig. 14.

5.4.1. Effect of piezoelectric fiber orientation angle

The FE model developed here is also capable of investigating the influence of variation of the piezoelectric fiber orientation angle (λ) in the obliquely reinforced 1–3 PZC constraining layer of the ACLD patches on their potential of attenuating the geometrically nonlinear vibrations of the FRMEE plates. To quantify the performance of the ACLD patch for controlling the large deflections of the FRMEE plate, a performance index (I_d) for computing the control authority of the obliquely reinforced 1–3 PZC constraining layer is defined as follows:

$$I_d = \frac{w_1(a/2,\ b/2,\ H/2) - w_{10}(a/2,\ b/2,\ H/2)}{w_1(a/2,\ b/2,\ H/2)} \times 100 \tag{44}$$

in which, w_1 and w_{10} are the magnitudes of the maximum amplitude at the first peak and the 10th peak, respectively. I_d measures the percentage suppression of the amplitude at the point (a/2, b/2, H/2) of the overall FRMEE plate undergoing nonlinear transient vibrations. For a particular value of the mechanical load and the maximum control voltage, Figs. 15 and 16 illustrate that the control authority (i.e. the performance index I_d) of the ACLD patch varies with the variation of the piezoelectric fiber orientation angle (λ) in the *xz*-plane while becoming maximum at λ = 0° for simply supported as well as clamped-clamped with antisymmetric cross-ply and antisymmetric angle-ply FRMEE plates, respectively. It may be

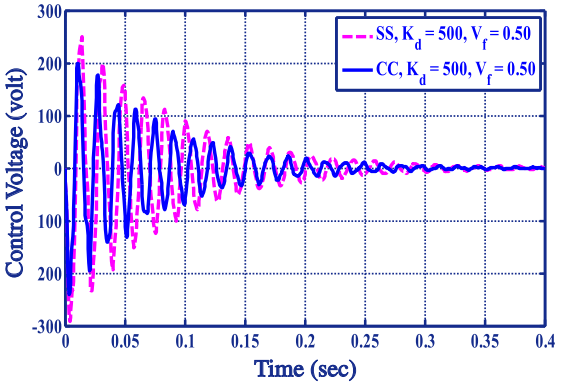

Fig. 9. Control voltages required for the ACLD of nonlinear transient vibrations of the simply supported and clamped-clamped antisymmetric cross-ply (0°/90°/0°/90°) FRMEE plates (a/H = 200, a = b, p = 1.8 kN/m^2).

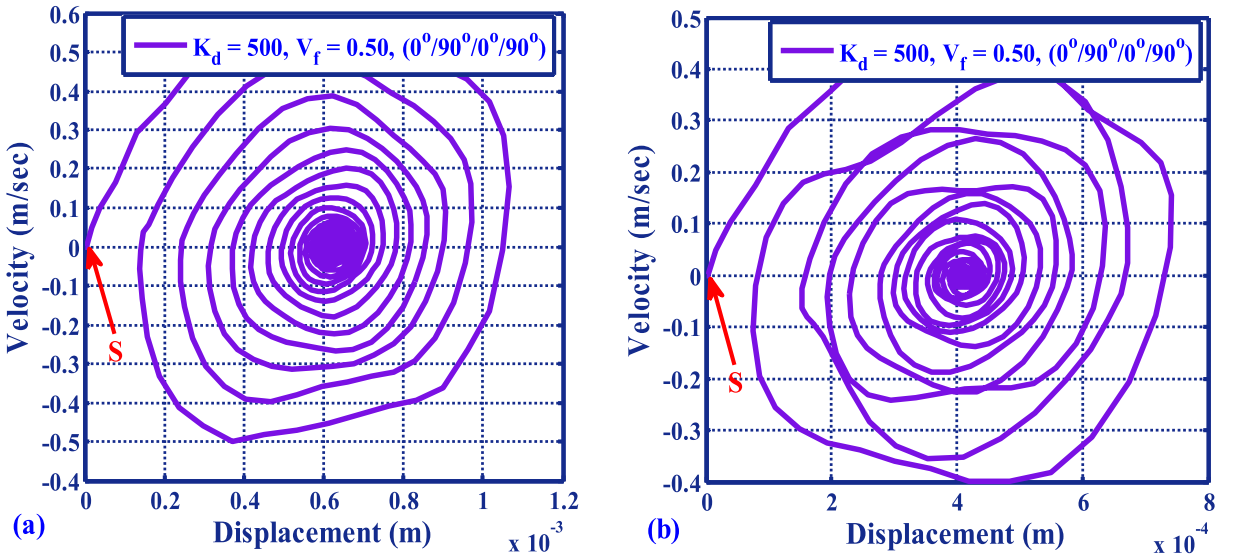

Fig. 10. Phase plots for a (a) simply supported and (b) clamped-clamped FRMEE plates when the ACLD patch controls the nonlinear vibrations of the plates ("S" is the starting point).

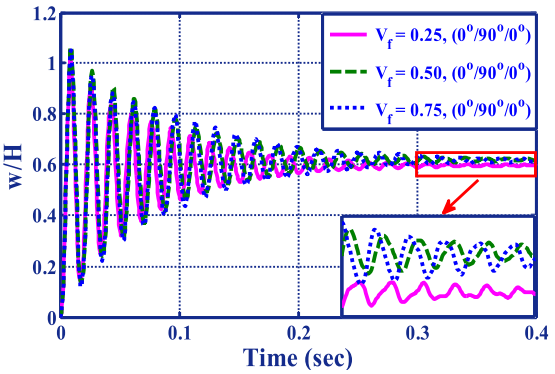

Fig. 11. Effect of fiber volume fraction (V_f) on the nonlinear transient responses of a simply supported symmetric cross-ply (0°/90°/0°) FRMEE plate undergoing ACLD (a/H = 200, a = b, p = 1.8 kN/m^2, max(V) = 275 V).

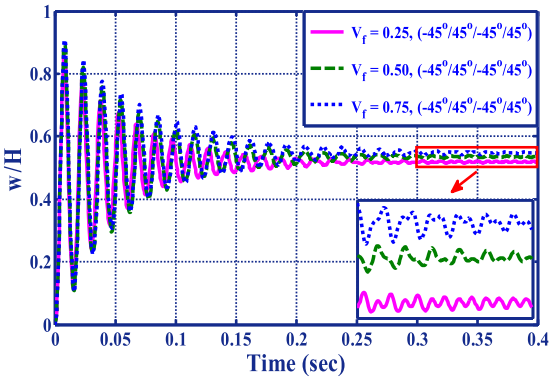

Fig. 12. Effect of fiber volume fraction (V_f) on the nonlinear transient responses of a simply supported antisymmetric angle-ply FRMEE plate undergoing ACLD (a/H = 200, a = b, p = 1.8 kN/m^2, max(V) = 235 V).

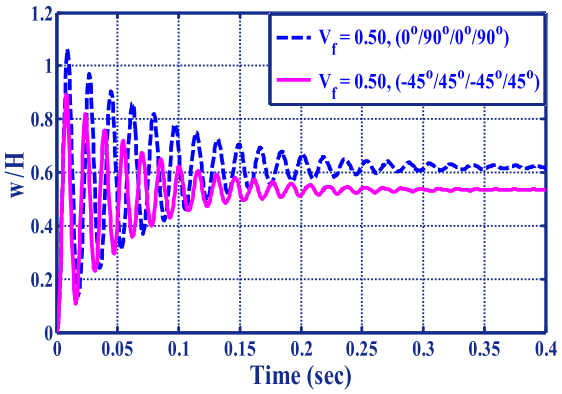

Fig. 13. Nonlinear transient responses for a simply supported cross-ply and angle-ply FRMEE plates (a/H = 200, a = b, p = 1.8 kN/m^2).

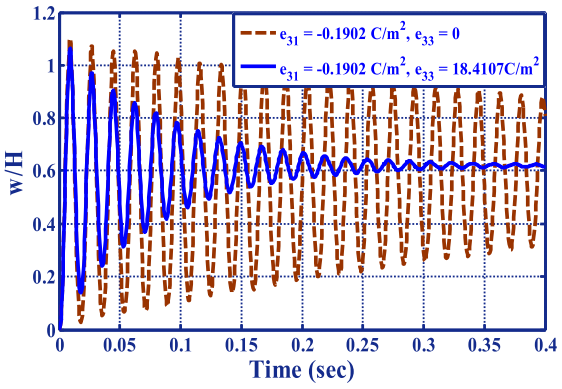

Fig. 14. Contributions of in-plane and transverse actuations by the PZC layer in the controlled response of the FRMEE plate undergoing geometrically nonlinear vibrations (a/H = 200, a = b, K_d = 500, p = 1.8 kN/m^2).

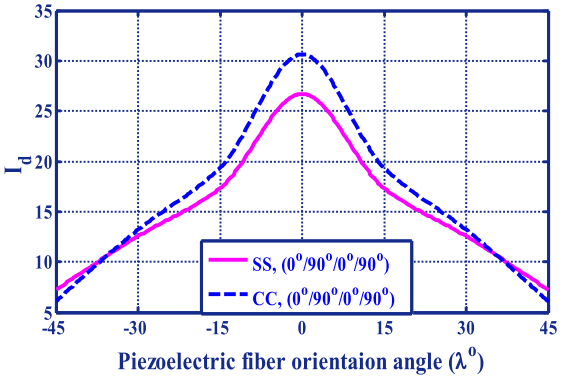

Fig. 15. Effect of variations of the piezoelectric fiber orientation angle (λ) in 1–3 PZC constraining layer of the ACLD patch on the control of active damping of geometrically nonlinear vibrations of the antisymmetric cross-ply FRMEE plates when the piezoelectric fibers are coplanar with the *xz*-plane (V_f = 0.50, p = 1.8 kN/m^2, max (V) = 285 V).

observed from these figures that the performance of the ACLD patch is independent of the sign of the piezoelectric fiber orientation angle (λ) in the 1–3 PZC constraining layer.

5.4.2. Effect of coupled fields

The effect of the electro-elastic and magneto-elastic coupled fields on the control of geometrically nonlinear transient vibrations has been studied by setting the corresponding matrices i.e., $[K_{t\phi}]$, $[K_{\phi\phi}]$ and/or $[K_{t\psi}]$, $[K_{\psi\psi}]$ to null matrices.

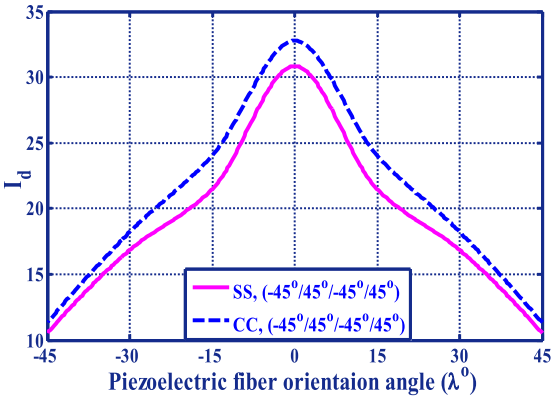

Fig. 16. Effect of variations of the piezoelectric fiber orientation angle (λ) in 1–3 PZC constraining layer of the ACLD patch on the control of active damping of geometrically nonlinear vibrations of the antisymmetric angle-ply FRMEE plates when the piezoelectric fibers are coplanar with the *xz*-plane (V_f = 0.50, p = 1.8 kN/m^2, max (V) = 285 V).

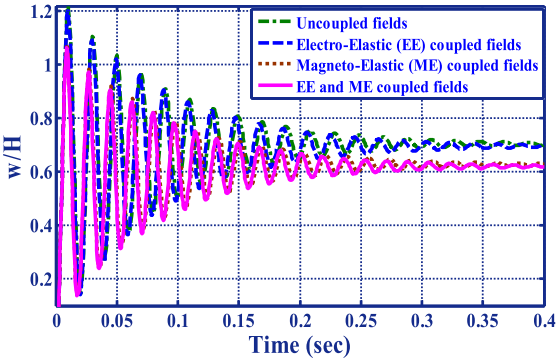

Fig. 17. Comparison of coupled and uncoupled controlled nonlinear transient responses of a simply supported cross-ply FRMEE plate undergoing ACLD (a/H = 200, a = b, K_d = 500, V_f = 0.50, p = 1.8 kN/m^2).

Fig. 17 demonstrates the effects on the controlled responses of a simply supported FRMEE plate. It is evident from this figure that the coupled fields cause a marginal stiffening effect on the FRMEE plate. It may also be noticed from this figure that the contribution of magneto-elastic coupled fields is higher than the electro-elastic coupled fields in contrary to the B/F/B and the F/B/F (B stands for $BaTiO_3$ and F stands for $CoFe_2O_4$) MEE plates studied by Kattimani and Ray [10] wherein the dominance of electro-elastic coupled fields has been observed. It may be due to the presence of both piezoelectric and piezomagnetic effect in each the layer of the FRMEE plate.

6. Conclusions

Control of geometrically nonlinear vibrations of the FRMEE plates integrated with the ACLD patch/patches has been investigated by deriving a three-dimensional FE model. The vertically/obliquely reinforced 1–3 PZC materials are considered as the candidate materials for the constraining layer of the ACLD treatment while the constrained viscoelastic layer is modeled by adapting the GHM approach in time domain. The FRMEE plates exhibit hardening type nonlinearity. The numerical results reveal that remarkable enhancement in the active damping characteristics of the FRMEE plates by the ACLD treatment over the passive damping for controlling the geometrically nonlinear vibrations has been achieved. The performance of the single ACLD patch placed at the center of the top surface of the FRMEE plates is significantly larger than that of the two patches placed at the opposite edges of the plates. The in-plane actuation by the 1–3 PZC layer for controlling the geometrically nonlinear vibrations is negligible while the vertical actuation of the vertically reinforced 1–3 PZC layer is mainly responsible for the active damping. The damping characteristic of the FRMEE plates increases with the decrease in the piezoelectric fiber volume fraction. The antisymmetric angle-ply FRMEE plates exhibit greater nonlinearity than the symmetric/antisymmetric cross-ply FRMEE plates.

The boundary conditions and the variation of the piezoelectric fiber orientation angle (λ) in the constraining layer significantly influence the performance of the ACLD patch for controlling the geometrically nonlinear vibrations of the FRMEE plates. The control authority of the patch becomes maximum for the vertically reinforced 1–3 PZC (i.e. $\lambda = 0°$) in the con-

straining layer of the ACLD patch. The electro-elastic and the magneto-elastic coupling exhibit marginal increase in the stiffening effect of the FRMEE plates while their contributions on controlling the nonlinear transient vibrations are negligible. The influence of the magneto-elastic coupled field is greater than that of the electro-elastic coupled field on the stiffening effect of the FRMEE plates.

Appendix A.

A.1. Transformation matrices

The transformation matrices $[Z_1]-[Z_5]$ appearing in Eqs. (5) and (6) are given by

$$[Z_1]=\begin{bmatrix}\bar{Z}_1 & \ddot{O} & \bar{O}\end{bmatrix},\ [Z_2]=\begin{bmatrix}\bar{Z}_2 & h_v\hat{I}_2 & (z-\frac{h}{2}-h_v)\hat{I}_2\end{bmatrix},\ [Z_3]=\begin{bmatrix}\bar{I} & \tilde{O} & \tilde{O} & \bar{Z}_3\end{bmatrix},$$

$$[Z_4]=\begin{bmatrix}\tilde{O} & \bar{I} & \tilde{O} & \bar{Z}_4\end{bmatrix},\ [Z_5]=\begin{bmatrix}\tilde{O} & \tilde{O} & \bar{I} & \bar{Z}_5\end{bmatrix}. \tag{A1}$$

where

$$\bar{Z}_1=\begin{bmatrix}z&0&0&0&0\\0&z&0&0&0\\0&0&0&1&2z\\0&0&z&0&0\end{bmatrix},\ \bar{Z}_2=\frac{h}{2}\begin{bmatrix}1&0&0&0&0\\0&1&0&0&0\\0&0&0&\frac{2}{h}&\frac{4}{h}z\\0&0&1&0&0\end{bmatrix},\ \bar{Z}_3=\begin{bmatrix}z&0&z^2&0\\0&z&0&z^2\end{bmatrix},\ \bar{Z}_4=\bar{Z}_5=\bar{Z}_3$$

$$\{\varepsilon_{bt}\}=\begin{bmatrix}\frac{\partial u_0}{\partial x} & \frac{\partial v_0}{\partial y} & 0 & \frac{\partial u_0}{\partial y}+\frac{\partial v_0}{\partial x}\end{bmatrix}^T,\{\varepsilon_{ts}\}=\begin{bmatrix}\frac{\partial w_0}{\partial x} & \frac{\partial w_0}{\partial y}\end{bmatrix}^T,$$

$$\{\varepsilon_{rb}\}=\begin{bmatrix}\frac{\partial\theta_x}{\partial x} & \frac{\partial\theta_y}{\partial y} & \frac{\partial\theta_x}{\partial y}+\frac{\partial\theta_y}{\partial x} & \theta_z & \phi_z & \frac{\partial\phi_x}{\partial x} & \frac{\partial\phi_y}{\partial y}\\ \frac{\partial\phi_x}{\partial y}+\frac{\partial\phi_y}{\partial x} & \frac{\partial\gamma_x}{\partial x} & \frac{\partial\gamma_y}{\partial y} & \frac{\partial\gamma_x}{\partial y}+\frac{\partial\gamma_y}{\partial x} & & & \end{bmatrix},$$

$$\{\varepsilon_{tbn}\}=\frac{1}{2}\begin{bmatrix}\left(\frac{dw_0}{dx}\right)^2 & \left(\frac{dw_0}{dy}\right)^2 & 0 & 2\left(\frac{dw_0}{dx}\right)^2\left(\frac{dw_0}{dy}\right)\end{bmatrix}^T \text{ and}$$

$$\{\varepsilon_{rs}\}=\begin{bmatrix}\theta_x & \theta_y & \phi_x & \phi_y & \gamma_x & \gamma_y & \frac{\partial\theta_z}{\partial x} & \frac{\partial\theta_z}{\partial y} & \frac{\partial\phi_z}{\partial x} & \frac{\partial\phi_z}{\partial y}\end{bmatrix}. \tag{A2}$$

A.2. Submatrices

The nodal strain-displacement matrices $[B_{tb}]$, $[B_{rb}]$, $[B_{ts}]$, $[B_{rs}]$, $[B_1]$ and $[B_2]$ appearing in Eq. (22) are given by

$$[B_{tb}]=\begin{bmatrix}B_{tb1} & B_{tb2} & \ldots & B_{tb8}\end{bmatrix},\ [B_{rb}]=\begin{bmatrix}B_{rb1} & B_{rb2} & \ldots & B_{rb8}\end{bmatrix},$$

$$[B_{ts}]=\begin{bmatrix}B_{ts1} & B_{ts2} & \ldots & B_{tb8}\end{bmatrix},\ [B_{rs}]=\begin{bmatrix}B_{rs1} & B_{rs2} & \ldots & B_{rs8}\end{bmatrix},$$

$$[B_1]=\begin{bmatrix}\frac{dw_0}{dx}&0&\frac{dw_0}{dy}&0\\0&\frac{dw_0}{dy}&\frac{dw_0}{dx}&0\end{bmatrix}^T,\ [B_2]=\begin{bmatrix}B_{21} & B_{22} & \ldots & B_{28}\end{bmatrix} \tag{A3}$$

The various submatrices $[B_{tbi}]$, $[B_{rbi}]$, $[B_{tsi}]$ and $[B_{rsi}]$ (i = 1, 2, 3,..., 8) are as follows

$$I=\begin{bmatrix}1&0&0\\0&1&0\\0&0&1\end{bmatrix},\quad \bar{I}=\begin{bmatrix}1&0\\0&1\end{bmatrix},\quad \tilde{I}=\begin{bmatrix}1&0&0\\0&1&0\\0&0&0\end{bmatrix},\quad \ddot{I}=\begin{bmatrix}0&0\\0&0\\0&1\end{bmatrix},\quad \hat{I}=\begin{bmatrix}1&0&0\\0&1&0\\0&0&0\\0&0&1\end{bmatrix}$$

$$[B_{tbi}]=\begin{bmatrix}\frac{\partial n_i}{\partial x}&0&0\\0&\frac{\partial n_i}{\partial y}&0\\0&\mathrm{d}&0\\\frac{\partial n_i}{\partial y}&\frac{\partial n_i}{\partial x}&0\end{bmatrix},\quad [B_{tsi}]=\begin{bmatrix}0&0&\frac{\partial n_i}{\partial x}\\0&0&\frac{\partial n_i}{\partial y}\end{bmatrix},\quad [B_{rbi}]=\begin{bmatrix}\hat{B}_{rbi}&\bar{0}&\bar{0}&\bar{0}\\\tilde{O}&I&\tilde{O}&\tilde{O}\\\bar{0}&\bar{0}&\hat{B}_{rbi}&\bar{0}\\\bar{0}&\bar{0}&\bar{0}&\hat{B}_{rbi}\end{bmatrix} \text{ and}$$

$$[B_{rsi}] = \begin{bmatrix} \tilde{I} & \ddot{I} & \tilde{0} \\ \tilde{0} & \bar{0} & I \\ \tilde{O} & \hat{B}_{rsi} & \bar{0}^T \\ \bar{0}^T & \hat{B}_{rsi} & \tilde{O} \end{bmatrix} \text{ in which, } \quad [\hat{B}_{rbi}] = \begin{bmatrix} \frac{\partial n_i}{\partial x} & 0 \\ 0 & \frac{\partial n_i}{\partial y} \\ \frac{\partial n_i}{\partial y} & \frac{\partial n_i}{\partial x} \end{bmatrix}, \quad [\hat{B}_{rsi}] = \begin{bmatrix} \frac{\partial n_i}{\partial x} & 0 & 0 \\ \frac{\partial n_i}{\partial y} & 0 & 0 \end{bmatrix} \tag{A4}$$

where $\tilde{0}$, $\bar{0}$, $\tilde{O}$, $\bar{O}$ and $\ddot{O}$ are the (3×3), (3×2), (2×2), (4×2) and (3×4) null matrices, respectively.

Appendix B

$$[M^e]\{\ddot{d}_t^e\} + [K_{tt}^e]\{d_t^e\} + [K_{tr}^e]\{d_r^e\} + [K_{tsv}^e]\int_0^t G(t-\tau)\frac{\partial}{\partial\tau}\{d_t^e\}d\tau + [K_{trsv}^e]\int_0^t G(t-\tau)\frac{\partial}{\partial\tau}\{d_r^e\}d\tau + [K_{t\phi}^e]\{\phi^e\} + [K_{t\psi}^e] \times \{\psi^e\} = \{F_t^e\} - \{F_{tp}^e\}V - \{F_{tpn}^e\}V \tag{B1}$$

$$[K_{tr}^e]^T\{d_t^e\} + [K_{rr}^e]\{d_r^e\} + [K_{trsv}^e]\int_0^t G(t-\tau)\frac{\partial}{\partial\tau}\{d_t^e\}d\tau + [K_{rrsv}^e]\int_0^t G(t-\tau)\frac{\partial}{\partial\tau}\{d_r^e\}d\tau + [K_{r\phi}^e]\{\phi^e\} + [K_{r\psi}^e]\{\psi^e\} = -\{F_{rp}^e\}V \tag{B2}$$

$$[K_{\phi t}^e]\{d_t^e\} + [K_{r\phi}^e]^T\{d_r^e\} - [K_{\phi\phi}^e]\{\phi^e\} = 0 \tag{B3}$$

$$[K_{\psi t}^e]\{d_t^e\} + [K_{r\psi}^e]^T\{d_r^e\} - [K_{\psi\psi}^e]\{\psi^e\} = 0 \tag{B4}$$

The various stiffness matrices appearing in Eqs. (B1)–(B4) are

$$[K_{tt}^e] = [K_{tb}^e] + [K_{ts}^e] + [K_{tbp}^e] + [K_{tsp}^e] + [K_{tbn}^e] + [K_{tbpn}^e],$$

$$[K_{tr}^e] = [K_{trb}^e] + [K_{trbn}^e] + [K_{trs}^e] + [K_{trbp}^e] + [K_{trbpn}^e] + [K_{trsp}^e],$$

$$[K_{rt}^e] = [K_{trb}^e]^T + \frac{1}{2}[K_{trbn}^e]^T + [K_{trs}^e]^T + [K_{rtbp}^e] + [K_{rtbpn}^e] + [K_{trsp}^e]^T,$$

$$[K_{rr}^e] = [K_{rrb}^e] + [K_{rrs}^e] + [K_{rrbp}^e] + [K_{rrsp}^e], \ [K_{t\phi}^e] = [K_{t\phi l}^e] + [K_{t\phi n}^e],$$

$$[K_{t\psi}^e] = [K_{t\psi l}^e] + [K_{t\psi n}^e], \ [K_{\phi t}^e] = [K_{t\phi l}^e]^T + \frac{1}{2}[K_{t\phi n}^e]^T, \ [K_{\psi t}^e] = [K_{t\psi l}^e]^T + \frac{1}{2}[K_{t\psi n}^e]^T$$

$$\{F_{tp}^e\} = \{F_{tpb}^e\} + \{F_{tps}^e\}, \ \{F_{rp}^e\} = \{F_{rpb}^e\} + \{F_{rps}^e\}, \ \{F_{tpn}^e\} = \int_0^{b_e}\int_0^{a_e}[B_2]^T[B_1]^T[F_{tbp}]dxdy,$$

$$\{F^e\} = \int_0^{b_e}\int_0^{a_e}[N_t]^T\{f\}dxdy, \tag{B5}$$

The elemental stiffness matrices appearing in Eq. (B5) corresponding to the bending stretching deformations are

$$[K_{t\phi l}^e] = \int_0^{a_e}\int_0^{b_e}[B_{tb}]^T[D_{t\phi}][N_\phi]dxdy, [K_{r\phi}^e] = \int_0^{a_e}\int_0^{b_e}[B_{rb}]^T[D_{r\phi}][N_\phi]dxdy,$$

$$[K_{t\phi n}^e] = \int_0^{a_e}\int_0^{b_e}[B_2]^T[B_1]^T[D_{t\phi}][N_\phi]dxdy, [K_{t\psi l}^e] = \int_0^{a_e}\int_0^{b_e}[B_{tb}]^T\{D_{t\psi}\}[N_\psi]dxdy,$$

$$[K_{r\psi}^e] = \int_0^{a_e}\int_0^{b_e}[B_{rb}]^T\{D_{t\psi}\}[N_\psi]dxdy, [K_{t\psi n}^e] = \int_0^{a_e}\int_0^{b_e}[B_2]^T[B_1]^T\{D_{t\psi}\}[N_\psi]dxdy,$$

$$[K_{\phi\phi}^e] = \int_0^{a_e}\int_0^{b_e}[N_\phi]^T[D_{\phi\phi}][N_\phi]dxdy, [K_{\psi\psi}^e] = \int_0^{a_e}\int_0^{b_e}[N_\psi]^T\{D_{\psi\psi}\}[N_\psi]dxdy,$$

$$[K^e_{tb}] = \int_0^{a_e}\int_0^{b_e} [B_{tb}]^T[D_{tb}][B_{tb}]dxdy, [K^e_{trb}] = \int_0^{a_e}\int_0^{b_e} [B_{tb}]^T[D_{trb}][B_{rb}]dxdy,$$

$$[K^e_{rrb}] = \int_0^{a_e}\int_0^{b_e} [B_{rb}]^T[D_{rrb}][B_{rb}]dxdy, [K^e_{trbn}] = \int_0^{b_e}\int_0^{a_e} [B_2]^T[B_1]^T[D_{trb}][B_{rb}]dxdy,$$

$$[M^e] = \int_0^{b_e}\int_0^{a_e} \bar{m}[N_t]^T[N_t]dxdy \text{ and } \bar{m} = \sum_{k=1}^{N+5}\int_{h_k}^{h_{k+1}} \rho^k dz$$

$$[K^e_{tbn}] = \int_0^{b_e}\int_0^{a_e} \left(\frac{1}{2}[B_{tb}]^T[D_{tb}][B_1][B_2] + [B_2]^T[B_1]^T[D_{tb}][B_{tb}] + \frac{1}{2}[B_2]^T[B_1]^T[D_{tb}][B_1][B_2]\right)dxdy,$$

$$[K^e_{tbp}] = \int_0^{a_e}\int_0^{b_e} ([B_{tb}]^T[D^p_{tb}][B_{tb}] + 2[B_{tb}]^T[D^p_{tbs}][B_{ts}])dxdy,$$

$$[K^e_{trbp}] = \int_0^{a_e}\int_0^{b_e} ([B_{tb}]^T[D^p_{trb}][B_{rb}] + [B_{tb}]^T[D^p_{trbs}][B_{rs}] + [B_{ts}]^T[D^p_{rtbs}]^T[B_{rb}])dxdy,$$

$$[K^e_{rrbp}] = \int_0^{a_e}\int_0^{b_e} ([B_{rb}]^T[D^p_{rrb}][B_{rb}] + 2[B_{rb}]^T[D^p_{rrbs}][B_{rs}])dxdy,$$

$$\{F^e_{tpb}\} = \int_0^{a_e}\int_0^{b_e} [B_{tb}]^T\{D^b_{tp}\}dxdy, \{F^e_{rpb}\} = \int_0^{a_e}\int_0^{b_e} [B_{rb}]^T\{D^b_{rp}\}dxdy. \tag{B6}$$

and those associated with the transverse shear deformations are

$$[K^e_{ts}] = \int_0^{a_e}\int_0^{b_e} [B_{ts}]^T[D_{ts}][B_{ts}]dxdy, [K^e_{trs}] = \int_0^{b_e}\int_0^{a_e} [B_{ts}]^T[D_{trs}][B_{rs}]dxdy,$$

$$[K^e_{rrs}] = \int_0^{b_e}\int_0^{a_e} [B_{rs}]^T[D_{rrs}][B_{rs}]dxdy, [K^e_{tsp}] = \int_0^{a_e}\int_0^{b_e} [B_{ts}]^T[D^p_{ts}][B_{ts}]dxdy,$$

$$[K^e_{trsp}] = \int_0^{a_e}\int_0^{b_e} [B_{ts}]^T[D^p_{trs}][B_{rs}]dxdy, [K^e_{rrsp}] = \int_0^{a_e}\int_0^{b_e} [B_{rs}]^T[D^p_{rrs}][B_{rs}]dxdy,$$

$$[K^e_{tsv}] = h_v\int_0^{b_e}\int_0^{a_e} [B_{ts}]^T[B_{ts}]dxdy, [K^e_{trsv}] = \int_0^{b_e}\int_0^{a_e} [B_{ts}]^T[D_{trsv}][B_{rs}]dxdy,$$

$$[K^e_{rrsv}] = \int_0^{b_e}\int_0^{a_e} [B_{rs}]^T[D_{rrsv}][B_{rs}]dxdy. \tag{B7}$$

The various rigidity matrices and rigidity vectors appearing in Eqs. (B6) and (B7) are given by

$$[D_{tb}] = \sum_{k=1}^{3}\int_{h_k}^{h_{k+1}} [\bar{C}^s_b]^k dz, [D_{trb}] = \sum_{k=1}^{3}\int_{h_k}^{h_{k+1}} [\bar{C}^s_b]^k[Z_1]dz, [D_{rrb}] = \sum_{k=1}^{3}\int_{h_k}^{h_{k+1}} [Z_1]^T[\bar{C}^s_b]^k[Z_1]dz,$$

$$[D_{ts}] = \sum_{k=1}^{3}\int_{h_k}^{h_{k+1}} [\bar{C}^s_s]^k dz, [D_{trs}] = \sum_{k=1}^{3}\int_{h_k}^{h_{k+1}} [\bar{C}^s_s]^k[Z_3]dz, [D_{rrs}] = \sum_{k=1}^{3}\int_{h_k}^{h_{k+1}} [Z_3]^T[\bar{C}^s_s]^k[Z_3]dz,$$

$$[D^p_{tb}] = \int_{h_5}^{h_6} [\bar{C}^p_b]dz, [D^p_{trb}] = \int_{h_5}^{h_6} [\bar{C}^p_b][Z_2]dz, [D^p_{rrb}] = \int_{h_5}^{h_6} [Z_2]^T[\bar{C}^p_b][Z_2]dz,$$

$$[D^p_{ts}] = \int_{h_5}^{h_6} [\bar{C}^p_s]dz, [D^p_{trs}] = \int_{h_5}^{h_6} [\bar{C}^p_s][Z_5]dz, [D^p_{rrs}] = \int_{h_5}^{h_6} [Z_2]^T[\bar{C}^p_s][Z_5]dz,$$

$$[D_{tsv}] = \int_{h_4}^{h_5} [\bar{C}^v_s]dz, [D_{trsv}] = \int_{h_4}^{h_5} [\bar{C}^v_s][Z_4]dz, [D_{rrsv}] = \int_{h_4}^{h_5} [Z_4]^T[\bar{C}^v_s][Z_4]dz,$$

$$[D^p_{tbs}] = \int_{h_5}^{h_6} [\bar{C}_{bs}]dz, [D^p_{trbs}] = \int_{h_5}^{h_6} [\bar{C}_{bs}][Z_5]dz, [D^p_{rtbs}] = \int_{h_5}^{h_6} [Z_2]^T[\bar{C}_{bs}]dz,$$

$$[D^p_{rrbs}] = \int_{h_5}^{h_6} [Z_2]^T[\bar{C}_{bs}][Z_5]dz, \{D^b_{tp}\} = \int_{h_5}^{h_6} \frac{1}{h_p}\{e^p_b\}dz, \{D^b_{rp}\} = \int_{h_5}^{h_6} \frac{1}{h_p}[Z_2]^T\{e^p_b\}dz,$$

$$\{D^s_{tp}\} = \int_{h_5}^{h_6} \frac{1}{h_p}\{e^p_s\}dz, \{D^s_{rp}\} = \int_{h_5}^{h_6} \frac{1}{h_p}[Z_5]^T\{e^p_s\}dz, \{D_{t\psi}\} = \int_{h_2}^{h_3} \{q^s_b\}\frac{1}{h}dz,$$

$$\{D_{t\phi}\} = \int_{h_3}^{h_4} \{e^s_b\}\frac{1}{h}[1 \quad 0]dz + \int_{h1}^{h_2} \{e^s_b\}\frac{1}{h}[0 \quad 1]dz,$$

$$\{D_{r\psi}\} = \int_{h_2}^{h_3} [Z_1]^T\{q^s_b\}\frac{1}{h}dz, \{D_{r\phi}\} = \int_{h_3}^{h_4} [z_1]^T\{e^s_b\}\frac{1}{h}[1 \quad 0]dz + \int_{h1}^{h_2} [z_1]^T\{e^s_b\}\frac{1}{h}[0 \quad 1]dz,$$

$$[D_{\phi\phi}] = \frac{\in^s_{33}}{h}\begin{bmatrix} 1 & 0 \\ 0 & 1 \end{bmatrix}, [D_{\psi\psi}] = \frac{1}{h}\mu_{33}. \tag{B8}$$

Appendix C

The various global stiffness matrices and force vectors appearing in Eqs. (36)–(38) are given by

$$[K_x] = [\bar{K}_{tt}] - [\bar{K}_{tr}][\bar{K}_{rr}]^{-1}[K_{tr}]^T, [K_z] = \alpha G^\infty[\bar{K}_{tr}][\bar{K}_{rr}]^{-1}[K_{trsv}]^T - \alpha G^\infty[K_{tsv}],$$

$$[K_{zr}] = \alpha G^\infty[\bar{K}_{tr}][\bar{K}_{rr}]^{-1}[K_{rrsv}] - \alpha G^\infty[K_{trsv}], [\bar{K}_{tt}] = [K_1] + G^\infty(1+\alpha)[K_{tsv}],$$

$$[\bar{K}_{tr}] = [K_2] + G^\infty(1+\alpha)[K_{trsv}]^T, [\bar{K}_{rt}] = [K_3] + G^\infty(1+\alpha)[K_{rrsv}]^T,$$

$$[\bar{K}_{rr}] = [K_4] + G^\infty(1+\alpha)[K_{rrsv}], [K_5] = [\bar{K}_{rr}]^{-1}[\bar{K}_{tr}]^T,$$

$$[K_6] = \alpha G^\infty[\bar{K}_{rr}]^{-1}[K_{trsv}]^T, [K_7] = I_{zr} - \alpha G^\infty[\bar{K}_{rr}]^{-1}[K_{rrsv}],$$

$$\{F^j_p\} = -[\bar{K}_{tr}][\bar{K}_{rr}]^{-1}\{F^j_{rp}\} + \{F^j_{tp}\} + \{F^j_{tpn}\}, \{F^j_{pz}\} = \hat{\omega}^2[\bar{K}_{rr}]^{-1}\{F^j_{rp}\}.$$

References

[1] E. Pan, Exact solution for simply supported and multilayered magneto-electro- elastic plates, ASME Trans. 68 (4) (2001) 608–618.
[2] E. Pan, P.R. Heyliger, Free vibrations of simply supported and multilayered magneto-electro-elastic plates, J. Sound Vib. 252 (3) (2002) 429–442.
[3] G.R. Buchanan, Layered versus multiphase magneto-electro-elastic composites, Compos.: Part B 35 (2004) 413–420.
[4] C.X. Xue, E. Pan, S.Y. Zhang, H.J. Chu, Large deflection of a rectangular magnetoelectroelastic thin plate, Mech. Res. Commun. 38 (2011) 518–523.
[5] J. Sladek, V. Sladek, S. Krahulec, E. Pan, The MLPG analysis of large deflections of magnetoelectroelastic plates, Eng. Anal. Boundary Elem. 37 (2013) 673–682.
[6] A. Alaimo, I. Benedetti, A. Milazzo, A finite element formulation for large deflection of multilayered magneto-electro-elastic plates, Compos. Struct. 107 (2013) 643–653.
[7] A. Milazzo, Large deflection of magneto-electro-elastic laminated plates, Appl. Math. Model. (2013), https://doi.org/10.1016/j.apm.2013.08.034.
[8] A. Milazzo, Variable kinematics models and finite elements for nonlinear analysis of multilayered smart plates, Compos. Struct. 122 (2015) 537–545.
[9] S.C. Kattimani, M.C. Ray, Active control of large amplitude vibrations of smart Magneto-electro-elastic doubly curved shells, Int. J. Mech. Mater. Des. (2014), https://doi.org/10.1007/s10999-014-9252-3.
[10] S.C. Kattimani, M.C. Ray, Smart damping of geometrically nonlinear vibrations of magneto-electro-elastic plates, Compos. Struct. 114 (2014) 51–63.
[11] H. Chen, W. Yu, A multiphysics model for magneto-electro-elastic laminates, Eur. J Mech. A/Solids 47 (2014) 23–44.
[12] A. Shooshtari, S. Razavi, Nonlinear vibration analysis of rectangular magneto-electro-elastic thin plates, Int. J. Eng. (IJE), Trans. A: Basics 28 (1) (2015) 136–144.
[13] Y. Zhou, J. Zhu, Vibration and bending analysis of multiferroic rectangular plates using third order shear deformation theory, Compos. Struct. 153 (2016) 712–723.
[14] S.C. Kattimani, Geometrically nonlinear vibration analysis of multiferroic composite plates and shells, Compos. Struct. 163 (2017) 185–194.
[15] J.Y. Li, M.L. Dunn, Micromechanics of magnetoelectroelastic composite materials: average fields and effective behavior, J. Intel. Mater. Syst. Struct. 9 (1998) 404–416.
[16] R. Grossingera, V. Giap, R. Duongb, Sato-Turtellia, The physics of magnetoelectric composites, J. Magn. Magn. Mater. 320 (2008) 1972–1977.
[17] M.F. Liu, An exact deformation analysis for the magneto-electro-elastic fiber-reinforced thin plate, Appl. Math. Model. 35 (2011) 2443–2461.
[18] J. Aboudi, Micromechanical analysis of fully coupled electro-magneto-thermo-elastic multiphase composites, Smart Mater. Struct. 10 (2001) 867–877.
[19] A.L. Kalamkarov, A.V. Georgiades, Micromechanical modelling of smart composite structures, Smart Mater. Struct. 11 (2002) 423–434.
[20] P. Naresh, A. Arockiarajan, An analytical model for predicting the effective properties of magneto-electro-elastic composites, Comput. Mater. Sci. 65 (2012) 19–28.

[21] Y. Wang, G.J. Weng, On Eshelby's S-tensor under various magneto-electro-elastic constitutive settings, and its application to multiferroic composites, J. Micromech. Mol. Phys. (2016), https://doi.org/10.1142/S2424913016400026.
[22] Y. Koutsawa, Overall thermo-magneto-electro-elastic properties of multiferroics composite materials with arbitrary heterogeneities spatial distributions, Compos. Struct. 133 (2015) 764–773.
[23] B.L. Wang, Y.W. Mai, Self-consistent analysis of coupled magnetoelectroelastic fracture – theoretical investigation and finite element verification, Comput. Methods Appl. Mech. Eng. 196 (13-16) (2017) 2044–2054.
[24] Y. Li, W. Feng, Z. Xu, Fracture analysis of cracked 2D planar and axisymmetric problems of magneto–electro-elastic materials by the MLPG coupled with FEM, Comput. Methods Appl. Mech. Eng. 198 (30-32) (2009) 2347–2359.
[25] A. Baz, J. Ro, Vibration control of plates with active constrained layer damping, Smart Mater. Struct. 5 (1996) 272–280.
[26] A. Baz, Robust control of active constrained layer damping, J. Sound Vib. 211 (3) (1998) 467–480.
[27] B. Azvine, G.R. Tomlinson, R.J. Wynne, Use of active constrained layer damping for controlling resonant, Smart Mater. Struct. 4 (1995) 1–6.
[28] M.C. Ray, A.K. Pradhan, Performance of vertically reinforced 1–3 piezoelectric composites for active damping of smart structures, Smart Mater. Struct. 15 (1) (2006) 631–641.
[29] M.C. Ray, N. Mallik, Finite element analysis of smart structures containing piezoelectric fiber reinforced composites actuators, AIAA J. 42 (7) (2004) 1398–1405.
[30] M.C. Ray, R.C. Batra, Vertically reinforced 1–3 piezoelectric composites for active damping of functionally graded plates, AIAA J. 45 (7) (2007) 1779–1784.
[31] J.X. Gao, Y.P. Shen, Active control of geometrically nonlinear transient vibration of composite plates with piezoelectric actuators, J. Sound Vib. 264 (2003) 911–928.
[32] M.C. Ray, J.N. Reddy, Active control of laminated cylindrical shells using piezoelectric fiber reinforced composites, Compos. Sci. Technol. 65 (2005) 1226–1236.
[33] S.R. Kumar, M.C. Ray, Active constrained layer damping of geometrically nonlinear vibrations of smart laminated composite sandwich plates using 1–3 piezoelectric composites, Int. J. Mech. Mater. Des. 8 (2012) 359–380.
[34] M.C. Ray, J. Oh, A. Baz, Active constrained layer damping of thin cylindrical shells, J. Sound Vib. 240 (5) (2001) 921–935.
[35] C. Chantalakhana, R. Stanway, Active constrained layer damping of clamped–clamped plate vibrations, J. Sound Vib. 241 (5) (2001) 755–777.
[36] P. Datta, M.C. Ray, Three-dimensional fractional derivative model of smart constrained layer damping treatment for composite plates, Compos. Struct. 156 (2016) 291–306.
[37] S.I. Kundalwal, M.C. Ray, Smart damping of fuzzy fiber reinforced composite plates using 1–3 piezoelectric composites, J. Sound Vib. 22 (6) (2016) 1526–1546.
[38] Y.H. Lim, V. Vasundara Varadan, Vijay K. Varadan, Closed loop finite element modelling of active constrained layer damping in the time domain analysis, Smart Mater. Struct. 11 (2002) 89–97.
[39] S.K. Sarangi, M.C. Ray, Smart damping of geometrically nonlinear vibrations of laminated composite beams using vertically reinforced 1–3 piezoelectric composites, Smart Mater. Struct. 19 (2010) 075020.
[40] D.J. Mc Tavish, P.C. Hughes, Modelling of linear viscoelastic space structures, J. Vib. Acoust. 115 (1) (1993) 103–113.